

Bifurcation analysis of a conceptual model for the Atlantic Meridional Overturning Circulation

John Bailie and Bernd Krauskopf

August 1, 2023

Abstract

The Atlantic Meridional Overturning Circulation (AMOC) distributes heat and salt into the Northern Hemisphere via a warm surface current toward the subpolar North Atlantic, where water sinks and returns southwards as a deep cold current. There is substantial evidence that the AMOC has slowed down over the last century. We introduce a conceptual box model for the evolution of salinity and temperature on the surface of the North Atlantic Ocean, subject to the influx of meltwater from the Greenland ice sheets. Our model, which extends a model due to Welander, describes the interaction between a surface box and a deep-water box of constant temperature and salinity, which may be convective or non-convective, depending on the density difference. Its two main parameters μ and η describe the influx of freshwater and the threshold density between the two boxes, respectively.

We use tools from bifurcation theory to analyse two cases of the model: the limiting case of instantaneous switching between convective or non-convective interaction, where the system is piecewise-smooth (PWS), and the full smooth model with more gradual switching. For the PWS model we perform a complete bifurcation analysis by deriving analytical expressions for all bifurcations. The resulting bifurcation diagram in the (μ, η) -plane identifies all regions of possible dynamics, which we show as phase portraits — both at typical parameter points, as well as at the different transitions between them. We also present the bifurcation diagram for the case of smooth switching and show how it arises from that of the PWS case. In this way, we determine exactly where one finds bistability and self-sustained oscillations of the AMOC in both versions of the model. In particular, our results show that oscillations between temperature and salinity on the surface North Atlantic Ocean disappear completely when the transition between the convective and non-convective regimes is too slow.

1 Introduction

The Atlantic Meridional Overturning Circulation (AMOC) is a large conveyor belt of water that spans the entire Atlantic Ocean. Light surface currents transport relatively warm and saline waters northward to high latitudes. Here, the water becomes denser, leading to downward convection and mixing with the deep ocean, and subsequent formation of deepwater masses. A deep current then transports this water back to lower latitudes, where it upwells to the surface, thus closing the circulation loop [1]. The strength of the AMOC is governed by the interplay between two proposed upwelling mechanisms [2, 3]. The first perspective is that turbulent mixing across surfaces of equal density results in the upwelling of deepwater to the surface ocean in low latitudes [4, 5]. The second perspective suggests that strong circumpolar winds induce upwelling in the South Atlantic Ocean [6]. Regardless of the mechanism, the process of deepwater formation is crucial in determining the shape and strength of the associated return current — making it a critical factor for the stability of the AMOC.

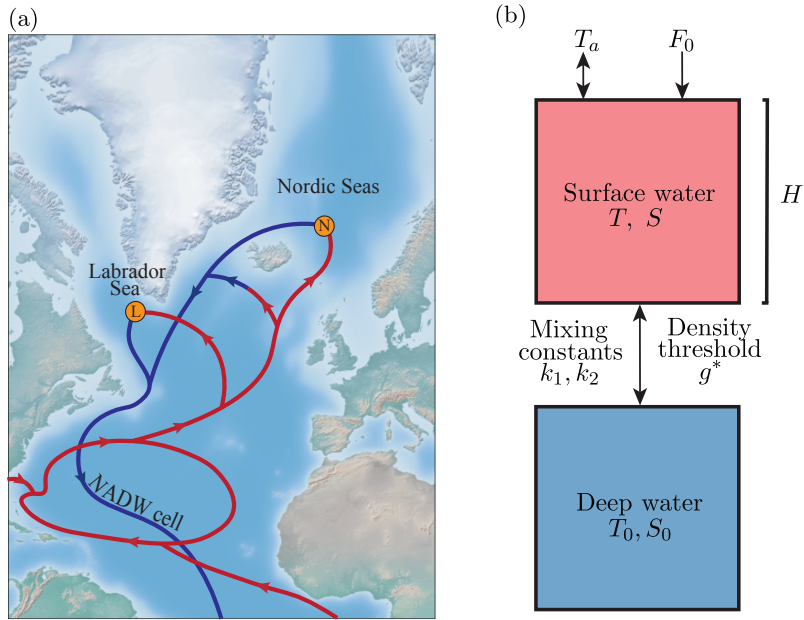


Figure 1: Panel (a) shows a simplified sketch of the North Atlantic component of the AMOC, inspired by [9]. The surface flow is displayed in red, and the NADW overturning cell in blue. Deepwater formation sites are denoted L and N in the Labrador sea and the Nordic seas, respectively. Panel (b) shows the two-box model setup for the interaction between surface water and cold deep water at the sites L and N.

This paper focuses on the deepwater formation sites in the North Atlantic. Specifically, as illustrated in Figure 1(a), the convection of highly saline water from the surface to the deep ocean in the Labrador and Nordic seas forms the North Atlantic Deep Water (NADW); it has an associated return current referred to as the NADW overturning cell. Several climate processes, such as salt rejection and atmospheric cooling, facilitate this convection by preconditioning the subpolar North Atlantic to have relatively high salinity [7]. Furthermore, an advective process transports saline water to the North Atlantic and, thus, stimulates the convection and formation of the NADW [8]. An inherent negative feedback loop forms: weaker convection results in a smaller NADW and, consequently, a weaker overturning cell. This weaker cell then advects less salt to the North Atlantic, further weakening the convection.

Evidence from proxy and sea surface temperature measurements indicate that the AMOC has weakened over the twentieth century [10]. There was also a particularly abrupt change in overturning strength during the 1970s [11] attributed to a large-scale influx of fresh water into the North Atlantic; this is known as the Great Salinity Anomaly and is linked to Arctic sea-ice export [12]. A weakened AMOC has significant consequences on the Earth's climate system since it leads to reduced northern heat transport, which lowers the oceanic and atmospheric temperature in the Northern hemisphere [13] via a weakening or even shutdown of the northern deepwater formation. Some significant implications drawn from simulations are a widespread cooling in Europe [10], the possible collapse of the North Atlantic plankton stocks [14], and a rise in the sea level [15]. As a result of external environmental factors, the AMOC is likely to weaken further, and a complete shutdown of the deep water formation in the Labrador Sea is a possibility [10]. In particular, meltwater from the melting Greenland ice sheets contributes to a large influx of freshwater into the subpolar North Atlantic [16]. As freshwater

is strictly non-saline, it dilutes the ocean surface water by lowering its salinity, thus, inhibiting the deep-water formation and, hence, the NADW overturning cell strength.

Of particular interest in this context is the modelling of the underlying deep water formation itself — with the aim of understanding the possible long-term behaviour of the AMOC in response to freshwater influx. Climate models form a hierarchy of complexity, and the choice of model depends on the nature of the question that is being asked. We study here a conceptual model of low complexity for investigating the AMOC in regard to deep water formation — specifically, from the class of box models that consider only a few variables in a relatively small number of interacting boxes, each representing a body of water of concern. While they are not designed to be used for prediction, box models are simple enough to be amenable to mathematical analysis, including with tools from dynamical systems theory [17].

The stability of the AMOC was first investigated by Stommel with a two-box model [18]; it considers the circulation between a subtropical box and a subpolar box, where a capillary flow represents the advection of water between the two boxes. Stommel’s model features three qualitatively different regimes. In the first regime, the AMOC is driven by salinity differences between the boxes, and surface currents move water toward the equator. Temperature differences are the main driver in the second regime, and the surface currents move water toward the poles. The final regime features bistability, where the AMOC may tip to either of the described equilibrium states. Stommel laid the foundation for several advective models, which add more boxes and physical processes; see, for example, [19, 20, 21].

A two-box model presented by Welander [22] attempts to describe self-sustained oscillations of temperature and salinity on the ocean surface in the presence of external forcing. The boxes interact by exchanging heat and salt via a mixing process. When the water in the surface box is sufficiently dense, the mixing is convective (strong). When the water in the boxes has comparable density, on the other hand, the mixing is non-convective (weak) and may happen via several climate processes, such as double-diffusion [23]. In this setup, an atmospheric basin with fixed properties interacts with the surface box, which is modelled by Newton’s transfer law. The model by Welander is described for two cases: when the transition between convective and non-convective mixing is modelled as a continuous change and, alternatively, when it is instantaneous and discontinuous. In both cases, self-sustained oscillations are observed, which are characterised by a convective and a non-convective phase. Welander’s model was re-examined by Leifeld [24] with the aim of formalising the previous analysis by using a modern approach of piecewise-smooth (PWS) dynamical systems. They undertook a preliminary stability analysis and made a first comparison between the smooth and non-smooth models; however, this work falls short of describing the full bifurcation picture and, to the best of our knowledge, there is as yet no complete analysis of the Welander model, nor any closely related models.

1.1 The adjusted Welander model

We take this as the starting point of our study of an *adjusted Welander model* that also considers the impact of a freshwater influx into the North Atlantic ocean. Following on from work in [25], where the external forcing enters in the form of Newton’s transfer law, we consider here a direct freshwater flux that dilutes the salinity in a surface ocean box at the North Atlantic, which is coupled to a box of deep water of constant lower temperature and salinity. As is illustrated by the schematic in Figure 1(b), the model takes the form of a planar system of ordinary differential equations for temperature T and

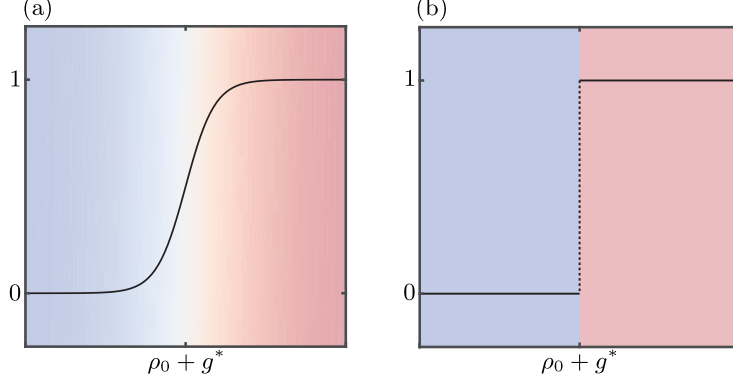


Figure 2: The switching functions $\mathcal{H}_\varepsilon(\rho - \rho_0 - g^*)$ with $\varepsilon = 0.1$ in panel (a) and $\varepsilon = 0$ in panel (b). Blue shading indicates mixing is mainly non-convective, and red shading that mixing is mainly convective. In the smooth transition region in panel (a), the colour changes from blue, via white, to red.

salinity S in the surface ocean box, which is given by

$$\begin{aligned} \frac{dT}{dt} &= -\gamma(T - T_a) - k_\varepsilon(\rho)(T - T_0), \\ \frac{dS}{dt} &= \frac{F_0}{H}S_0 - k_\varepsilon(\rho)(S - S_0). \end{aligned} \quad (1)$$

The atmosphere externally drives the surface ocean box to a thermal equilibrium T_a at rate γ , which is Newton's transfer law. The salinity, on the other hand, is directly forced by the freshwater flux F_0 at the rate $\frac{F_0}{H}S_0$, where H is the depth of the surface ocean box. Moreover, T_0 and S_0 are the (fixed) temperature and salinity of the deep-ocean box that drive T and S , respectively, as given by the convective exchange function k_ε . This function determines the coefficient for Newton's transfer law and takes as its argument the density ρ of the surface ocean box given (in linear approximation) by

$$\frac{\rho}{\rho_0} = 1 + \alpha_S(S - S_0) - \alpha_T(T - T_0). \quad (2)$$

Here, the constant ρ_0 is the density of the bottom box, and the coefficients α_S and α_T are, respectively, the saline expansion and thermal compression constants [17].

The convective exchange function is a key ingredient in (1) and describes the transition between the two regimes when the vertical mixing between the two boxes is non-convective at rate $k_1 > 0$ and when it is convective at rate $k_2 > k_1$. This transition is modeled in its general form as

$$k_\varepsilon(\rho) = k_1 + \mathcal{H}_\varepsilon(\rho - \rho_0 - g^*)(k_2 - k_1), \quad (3)$$

where \mathcal{H}_ε is a suitable switching function from zero to one, whose switching time depends on the switching-time parameter ε . Hence, when the density difference $\rho - \rho_0$ is (sufficiently) greater than the density threshold g^* , mixing between the boxes is mainly convective; on the other hand, it is mainly non-convective when $\rho - \rho_0$ is (sufficiently) smaller than g^* . Different switching functions have been used in the literature [24, 20], including those based on the arctan function. In this paper, we define \mathcal{H}_ε as

$$\mathcal{H}_\varepsilon(u) = \frac{1}{2} \left(1 + \tanh \left(\frac{u}{\varepsilon} \right) \right). \quad (4)$$

Note that \mathcal{H}_ε has a switching time of order $\varepsilon > 0$ and maximal rate of switching $\frac{1}{\varepsilon}$ given by the derivative of \mathcal{H}_ε at zero. Moreover, the limiting case for $\varepsilon \rightarrow 0$ is an instantaneous switch, represented by the Heaviside function \mathcal{H}_0 . Figure 2 shows the resulting convective exchange functions $k_\varepsilon(\rho)$ from (3) for $\varepsilon = 0.1$ and $\varepsilon = 0$.

The adjusted Welander model in the form (1) has ten parameters, making a direct analysis impractical. The first step in our analysis is to non-dimensionalise the system by introducing rescaled temperature, salinity and time

$$x = \frac{T - T_0}{T_a - T_0}, \quad y = \frac{\alpha_S(S - S_0)}{\alpha_T(T_a - T_0)}, \quad \tau = \gamma t, \quad (5)$$

and parameters

$$\kappa_i = \frac{k_i}{\gamma}, \quad \mu = \frac{F_0 S_0 \alpha_S}{\gamma \alpha_T (T_a - T_0) H}, \quad \eta = \frac{g^*(\kappa_2 - \kappa_1)}{\gamma \alpha_T (T_a - T_0) \rho_0}. \quad (6)$$

This transforms (1) into

$$\begin{aligned} \dot{x} &= 1 - (1 + \kappa_1 + \mathcal{H}_\varepsilon(y - x - \eta)(\kappa_2 - \kappa_1))x, \\ \dot{y} &= \mu - (\kappa_1 + \mathcal{H}_\varepsilon(y - x - \eta)(\kappa_2 - \kappa_1))y, \end{aligned} \quad (7)$$

where the dot represents the derivative with respect to the rescaled time.

1.2 Outline of the work

The adjusted Welander model in the form (7) is our central object of study. We first perform in Section 2 a (non-smooth) bifurcation analysis for the limiting case of system (7) with the Heaviside switching function \mathcal{H}_0 . Specifically, we determine and catalogue all of the possible dynamics, by presenting analytical expressions for all codimension-one and codimension-two bifurcations; the corresponding proofs and derivations can be found in Appendix A. The rescaled freshwater flux μ and density threshold η are the bifurcation parameters, and we show the complete bifurcation diagram in the (μ, η) -plane for a reasonable choice of the vertical mixing coefficients $0 < \kappa_1 < \kappa_2$. Moreover, we present representative phase portraits in the (x, y) -plane for all open regions, of which there are eight, for the different types of transitions of codimension one between them, as well as at the five codimension-two points that organise the bifurcation diagram. In particular, we identify the parameter regime where the system exhibits bistability between states, where deep-water convection is either substantial or shut down, which is characteristic behaviour of several models of different complexity [8]. Moreover, we determine the parameter regime with self-sustained relaxation-type oscillations that have been observed in [25] and also in Welander's original work [20]. In addition to this earlier work, we determine this region analytically and clarify the nature of the different possible transitions to/from this oscillatory regime. Our results also show that the bifurcation diagram in the (μ, η) -plane is topologically the same for any fixed $0 < \kappa_1 < \kappa_2$.

Section 3 is then concerned with the smooth case of system (7) with \mathcal{H}_ε for $\varepsilon > 0$. Here we first present the bifurcation diagram in the (μ, η) -plane for $\varepsilon = 0.1$ (for the same choice of $0 < \kappa_1 < \kappa_2$). This requires computing the relevant bifurcation curves by making use of established bifurcation theory [26] in conjunction with the continuation software package AUTO-07p [27]. We focus here on the main parameter regimes, especially those that feature bistability and self-sustained oscillations, for which we show representative phase portraits. We then present a partial bifurcation analysis in (μ, η, ε) -space that clarifies the convergence of the bifurcation diagram in the (μ, η) -plane as ε approaches 0. Moreover, we show that there is a codimension-three bifurcation at a quite low value of the switching-time parameter ε , at which the region with self-sustained oscillations completely disappears from the

(μ, η) -plane. In other words, the switching between the regimes with strong convective mixing and with weak non-convective mixing needs to be sufficiently fast for relaxation-type oscillations to occur in the adjusted Welander model (7). In particular, this shows the relevance of the non-smooth limiting system with \mathcal{H}_0 for explaining this oscillatory behaviour.

In the final Section 4 we summarise our findings, briefly discuss their significance for the dynamics of AMOC, and point out some direction for future work.

2 Bifurcation analysis of the PWS model for $\varepsilon = 0$

In the limiting case of an instantaneous transition with the transition function \mathcal{H}_0 from (4), system (7) reduces to the piecewise-smooth linear Filippov system

$$\begin{pmatrix} \dot{x} \\ \dot{y} \end{pmatrix} = \begin{cases} f_1(x, y), & y < x + \eta \\ f_2(x, y), & y > x + \eta \end{cases} \quad (8)$$

with

$$f_i(x, y) = \begin{pmatrix} 1 - (1 + \kappa_i)x \\ \mu - \kappa_i y \end{pmatrix}. \quad (9)$$

The switching manifold

$$\Sigma = \{(x, y) \in \mathbb{R}^2, \quad y = x + \eta\} \quad (10)$$

is a straight line that partitions the phase space of (8) into the open regions

$$R_1 = \{(x, y) \in \mathbb{R}^2, \quad y < x + \eta\}, \quad (11)$$

$$R_2 = \{(x, y) \in \mathbb{R}^2, \quad y > x + \eta\}, \quad (12)$$

where f_1 and f_2 apply, respectively.

We now perform a bifurcation analysis of the piecewise-smooth AMOC model (8). To this end, we use tools from the bifurcation theory for this class of non-smooth systems from the relevant literature [28, 29, 30], which we largely follow also in terms of notation and where more details can be found. More specifically, we determine analytic expressions for all (non-smooth) bifurcations, which is possible because of the simple expression for the switching manifold, and the fact that f_1 and f_2 are linear. We present these results in the form of propositions, whose proofs can be found in Appendix A. The associated curves of codimension-one bifurcations divide the (μ, η) -plane into eight open regions, denoted I – VIII. We also present the corresponding phase portraits in the (μ, η) -plane, as well as those at the different types of bifurcations. The vertical mixing coefficients are fixed here to $\kappa_1 = 0.1$ and $\kappa_2 = 1.0$. This choice is suitable for our purposes and in the realistic range [25], yet slightly different from the values found in the literature [24, 22]. Moreover, as can be seen from the expressions in Section 2.3, the bifurcation diagram in the (μ, η) -plane is qualitatively the same for any $0 < \kappa_1 < \kappa_2$.

2.1 Sliding properties and pseudo-equilibria

We start by introducing some relevant notions from the theory of PWS systems. An equilibrium p_i of the vector field f_i that lies in region R_i is an equilibrium of the overall system and called *admissible*. An important part of the bifurcation theory of planar Filippov systems is the interaction of equilibria and other invariant objects of f_1 and f_2 with the switching manifold Σ [28]. First of all, orbits may

cross the switching manifold at the *crossing segment* $\Sigma_c \subset \Sigma$, along which the vector fields f_1 and f_2 are both transverse and have the same sign. The set of points where f_1 and f_2 are transversal but have opposite signs is the *sliding segment* $\Sigma_s \subset \Sigma$, which we also refer to as Σ_s^a when it is attracting and as Σ_s^r when it is repelling. These different segments of the switching manifold are bounded by *tangency points* F_1 and F_2 , where either f_1 or f_2 is tangent to Σ , respectively. Generically, such a tangency of f_i is quadratic and isolated, and it is called visible if nearby parabolic orbits lie in R_i , and invisible otherwise. For system (8) we have the following.

Proposition 1 (Tangency points and sliding segments). *System (8) has a single sliding segment Σ_s that is delimited by two tangency points F_1 and F_2 at*

$$F_i = \begin{pmatrix} 1 - \mu + \eta\kappa_i \\ 1 - \mu + (1 + \kappa_i)\eta \end{pmatrix} \in \Sigma, \quad (13)$$

which are quadratic when

$$\mu + (\mu - \eta - 1)\kappa_i - \eta\kappa_i^2 \neq 0. \quad (14)$$

The (quadratic) tangency point F_1 is visible for

$$\mu + (\mu - \eta - 1)\kappa_i - \eta\kappa_i^2 < 0, \quad (15)$$

and the (quadratic) tangency point F_2 is visible for

$$\mu + (\mu - \eta - 1)\kappa_i - \eta\kappa_i^2 > 0. \quad (16)$$

Otherwise, the (quadratic) tangency at F_i is invisible. For $\eta \neq 0$, system (8) has a sliding segment Σ_s . When $\eta > 0$ the sliding segment is attracting, denoted Σ_s^a and given by

$$\Sigma_s^a = \{s \in \Sigma, F_1 < s < F_2\}, \quad (17)$$

and when $\eta < 0$ it is repelling, denoted Σ_s^r and given by

$$\Sigma_s^r = \{s \in \Sigma, F_2 < s < F_1\}. \quad (18)$$

Here, in a slight abuse of notation, we mean the ordering on the line Σ_s , as given by the x -component.

A crucial ingredient of the theory is the extension of the flow to the sliding segment Σ_s by defining the sliding vector field f_s . This is achieved with Filippov's convex method by forming a weighted sum of the adjoining vector fields f_1 and f_2 such that f_s is in the direction of (the tangent to) Σ_s [28, 29, 30]. With this definition, a PWS orbit is the union of orbit segments induced by the vector fields f_1 on R_1 , f_2 on R_2 , and f_s on Σ_s . Moreover, every point of the phase plane lies on a unique PWS orbit of the planar Filippov system; see [30] for details. Orbits that remain in $R_1 \cup R_2 \cup \Sigma_c$ are called *regular*, and orbits with segments on Σ_s are called *sliding orbits*. Here we use a common convention that sliding orbits continue into R_1 or R_2 when the end of the sliding segment Σ_s is reached (in forward or backward time, respectively, by following the trajectory from the respective tangency point) [30, 31]. However, the end of Σ_s may not be reached because the sliding vector field may have equilibria, called *pseudo-equilibria*, which are referred to as *admissible* when they lie Σ_s .

The properties of all equilibria of system (8) can be stated as follows.

Proposition 2 (Equilibria, sliding vector field and pseudo-equilibria). *System (8) has the following equilibria and pseudo-equilibria for $0 < \kappa_1 < \kappa_2$.*

1. The vector field f_i has the stable nodal equilibrium

$$p_i = \left(\frac{1}{1 + \kappa_i}, \frac{\mu}{\kappa_i} \right). \quad (19)$$

The equilibrium p_1 is admissible when

$$\eta > \frac{\mu}{\kappa_1} - \frac{1}{1 + \kappa_1}, \quad (20)$$

and p_2 is admissible when

$$\eta < \frac{\mu}{\kappa_2} - \frac{1}{1 + \kappa_2}. \quad (21)$$

The admissible equilibrium p_i has a strong stable manifold $W^{ss}(p_i)$ defined by the piecewise-smooth orbit along the linear strong stable direction $W_{loc}^{ss} = \text{span} \begin{pmatrix} 1 \\ 0 \end{pmatrix}$.

2. The sliding vector field defined on the sliding segment Σ_s is given by

$$f_s(x) = \frac{1}{\eta} (\mu + (\mu - \kappa_2 \eta - 1)x + x^2) \begin{pmatrix} 1 \\ 1 \end{pmatrix}, \quad (22)$$

where Σ is parametrised by x .

3. There are two pseudo-equilibria, that is, equilibria of f_s , given by

$$q^\pm = \frac{1}{2} \left(1 - \mu - \eta \pm \sqrt{(\eta + \mu + 1)^2 - 4\mu} \right) \begin{pmatrix} 1 \\ 1 \end{pmatrix} + \begin{pmatrix} 0 \\ \eta \end{pmatrix}. \quad (23)$$

When $\eta > 0$, the pseudo-equilibrium q^- is asymptotically unstable and q^+ is asymptotically stable on Σ_s . On the other hand, when $\eta < 0$, the pseudo-equilibrium q^+ is asymptotically unstable and q^- is asymptotically stable on Σ_s . The admissibility of these pseudo-equilibria is presented and described in Section 2.2.

Global invariant manifolds of admissible equilibria are defined in complete analogy to those of smooth systems, but with regard to the piecewise-smooth flow φ^t constructed in [30]. Each admissible equilibrium $p_i \in R_i$ of system (8) is attracting with real eigenvalues and, hence, has a strong stable manifold $W^{ss}(p_i)$ consisting of the two orbits that approach p_i tangent to the strong eigenspace. Since system (8) is piecewise linear, $W^{ss}(p_i)$ is actually a straight line locally near p_i ; however, this is not the case globally since the strong stable manifold typically crosses the switching manifold Σ .

We also consider here global invariant manifolds of admissible pseudo-equilibria, which we define as follows. If $q \in \Sigma_s$ is a saddle pseudo-equilibrium then its stable manifold $W^s(p)$ or unstable manifold $W^u(p)$ is the union of the two *arriving or departing orbits* in R_1 and R_2 , consisting of points that reach q under the piecewise-smooth flow φ^t in finite forward or backward time, respectively. The saddle pseudo-equilibrium q then also has associated *generalised (un)stable manifolds* $W_g^u(q)$ or $W_g^s(q)$. These generalised manifolds consist of segments on Σ_s of points that converge to q under the sliding flow (in backward and forward time, respectively), together with their globalisation under φ^t , which generally consists of departing and arriving orbits to tangency points that bound Σ_s . When an admissible pseudo-equilibrium q is a nodal attractor, its arriving orbits form the strong stable manifold $W^{ss}(p)$; similarly, a nodal repeller $q \in \Sigma_s$ has the strong unstable manifold $W^{uu}(p)$ consisting of its pair of departing orbits.

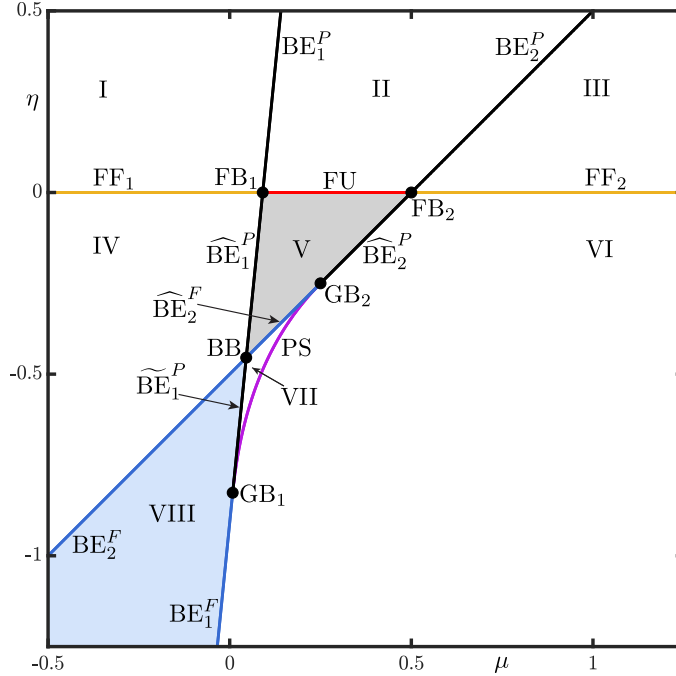


Figure 3: Two-parameter bifurcation diagram of system (8) in the (μ, η) -plane with $\kappa_1 = 0.1$ and $\kappa_2 = 1.0$. The curves of boundary equilibrium bifurcation BE_1 and BE_2 , fold-fold bifurcation FF , and pseudo-saddle-node bifurcation PS from Proposition 3 bound regions I to VIII with structurally stable phase portraits shown in Figures 4–6. Grey shading indicates the existence of a (crossing) periodic orbit, and blue shading bistability between equilibria. These curves intersect at the codimension-two points FB_1 , FB_2 , BB , GB_1 , and GB_2 from Proposition 4, which generates segments of different bifurcation types shown in Figures 7–11. Specifically, the curves BE_1 and BE_2 consist of segments BE_1^P , BE_2^P , \widehat{BE}_1^P , \widehat{BE}_2^P and \widetilde{BE}_1^P of persistence boundary equilibrium bifurcation, and BE_1^F , BE_2^F and \widehat{BE}_2^F of non-smooth fold boundary equilibrium bifurcation. The curve FF consists of segments FF_1 and FF_2 of fold-fold bifurcation and FU of fused-focus bifurcation.

2.2 Bifurcation diagram and structurally stable phase portraits

The bifurcation diagram of system (8) consists of curves of (piecewise-smooth) bifurcations that divide the (μ, η) -plane into eight open regions I to VIII, which are equivalence classes of topological equivalence where the phase portraits are structurally stable. This classification is based on the following common notion [30, 31]: two planar Filippov systems f and \tilde{f} with switching manifolds Σ and $\tilde{\Sigma}$, respectively, are *topologically equivalent* if there exists an orientation preserving homeomorphism $h : \mathbb{R}^2 \rightarrow \mathbb{R}^2$ that maps Σ to $\tilde{\Sigma}$ and orbits of f to orbits of \tilde{f} . Note that this definition is a direct and natural extension of that for smooth dynamical systems. In particular, a bifurcation of a planar Filippov system concerns a topological change, and its codimension is given (colloquially speaking) by the number of parameters one needs to find it generically at an isolated point. More information and formal definitions can be found as part of the broad classification in [31] of discontinuity-induced bifurcations in planar Filippov systems.

Figure 3 shows the bifurcation diagram of system (8) in the (μ, η) -plane, for the fixed values $\kappa_1 = 0.1$ and $\kappa_2 = 1.0$ of the vertical mixing rates, with the regions I to VIII. Their boundaries are formed by bifurcation curves BE_1 and BE_2 of boundary equilibrium bifurcation, FF of fold-fold

bifurcation and PS of pseudo-saddle-node bifurcation that are formally presented and determined in Proposition 3. More precisely, these curves cross or meet at codimension-two bifurcation points FB_1 , FB_2 , BB , GB_1 , and GB_2 . As is spelled out in Proposition 4, these points divide the curves of codimension-one bifurcations into the segments of different bifurcation types that are shown and labeled in Figure 3.

We first present and discuss the structurally stable phase portraits of system (8) in regions I to VIII; the different bifurcations between them are analysed and illustrated in subsequent sections. The eight cases of phase portraits are shown in Figures 4–6 in a suitable part of the (x, y) -plane. In every phase portrait, the switching manifold Σ appears as a straight grey line that partitions phase space into the open regions R_1 and R_2 . Admissible equilibria of system (8) are shown in black, and non-admissible equilibria in grey. Non-admissible equilibria outside the frame of interest (far away from the switching manifold) are not shown. There exists a sliding segment in each region: attracting sliding segments Σ_s^a are coloured blue, and repelling sliding segments Σ_s^r are coloured orange. In either case, the sliding segment is bounded by the quadratic tangency points F_1 and F_2 , which are coloured cyan when visible and grey when invisible. Admissible pseudo-equilibria q^- and q^+ are coloured by their stability: stable pseudo-equilibria are green, and unstable pseudo-equilibria are red. Admissible equilibria and pseudo-equilibria may have (strong) invariant manifolds that are coloured blue when stable and red when unstable. Some representative trajectories are shown in black, and they were obtained numerically with an integrator based on event-detection, as described in [32].

Figure 4 presents phase portraits of system (8) in regions I to III, which all feature an attracting sliding segment Σ_s^a . In the phase portrait in region I, shown in panel (a), Σ_s^a is bounded by a visible quadratic tangency point F_1 on the left and an invisible quadratic tangency point F_2 on the right. Neither of the pseudo-equilibria q^- and q^+ are on Σ_s^a and, hence, they are non-admissible (and not shown). The equilibrium p_2 lies in region R_1 and is non-admissible, while $p_1 \in R_1$ is admissible and a global attractor. Orbits in R_1 and R_2 are either regular and converge to p_1 or hit the attracting sliding segment Σ_s^a , along which sliding orbits approach F_1 and then depart into R_1 to converge to p_1 . Note, that the strong stable manifold $W^{ss}(p_1)$ of p_1 is composed of a horizontal component in R_1 and the corresponding arriving orbit in R_2 . Crossing the segment BE_1^P of boundary equilibrium bifurcation results in p_1 becoming non-admissible by moving into R_2 through F_1 ; at the same time, a pseudo-equilibrium $q^+ \in \Sigma_s^a$ emerges from F_1 , where the tangency is now invisible. The resulting phase portrait in region II is shown in Figure 4(b1) with a magnification near the sliding segment in panel (b2). The pseudo-equilibrium q^+ is a global attractor: all orbits in R_1 and R_2 hit the sliding segment Σ_s^a , along which the sliding orbits converge to q^+ . Moreover, q^+ has the strong stable manifold $W^{ss}(q^+)$, consisting of the two arriving orbits to q^+ from within R_1 and R_2 , respectively; see panel (b2). When the segment BE_2^P is crossed there is again a boundary equilibrium bifurcation, but now of p_2 at F_2 : as Figure 4(c) shows, in region III the pseudo-equilibrium q^+ moved off Σ_s^a through F_2 , and p_2 with strong stable manifold $W^{ss}(p_2)$ is now admissible and the global attractor.

Phase portraits in regions IV to VI are presented Figure 5; as was the case for regions I to III, this also concerns the transition from p_1 to p_2 being the global attractor, with the difference that there is now a repelling sliding segment Σ_s^r . In the phase portrait in region IV, shown in panel (a), Σ_s^r is bounded by an invisible quadratic tangency point F_2 on the left and by a visible quadratic tangency point F_1 on the right; the pseudo-equilibria q^- and q^+ are on Σ_c and non-admissible (and not shown). The only admissible equilibrium is $p_1 \in R_1$, and it is a global attractor. Sliding orbits on Σ_s^r approach F_2 , where they depart into R_1 and converge to p_1 ; however, in contrast to region III, no forward orbits hit Σ_s^r as this sliding segment is repelling. When crossing segment \widehat{BE}_1^P , we find again a (persistence) boundary equilibrium bifurcation where p_1 moves through F_1 and becomes non-admissible. As Figure 5(b1) and the magnification in panel (b2) show, in region V this results again

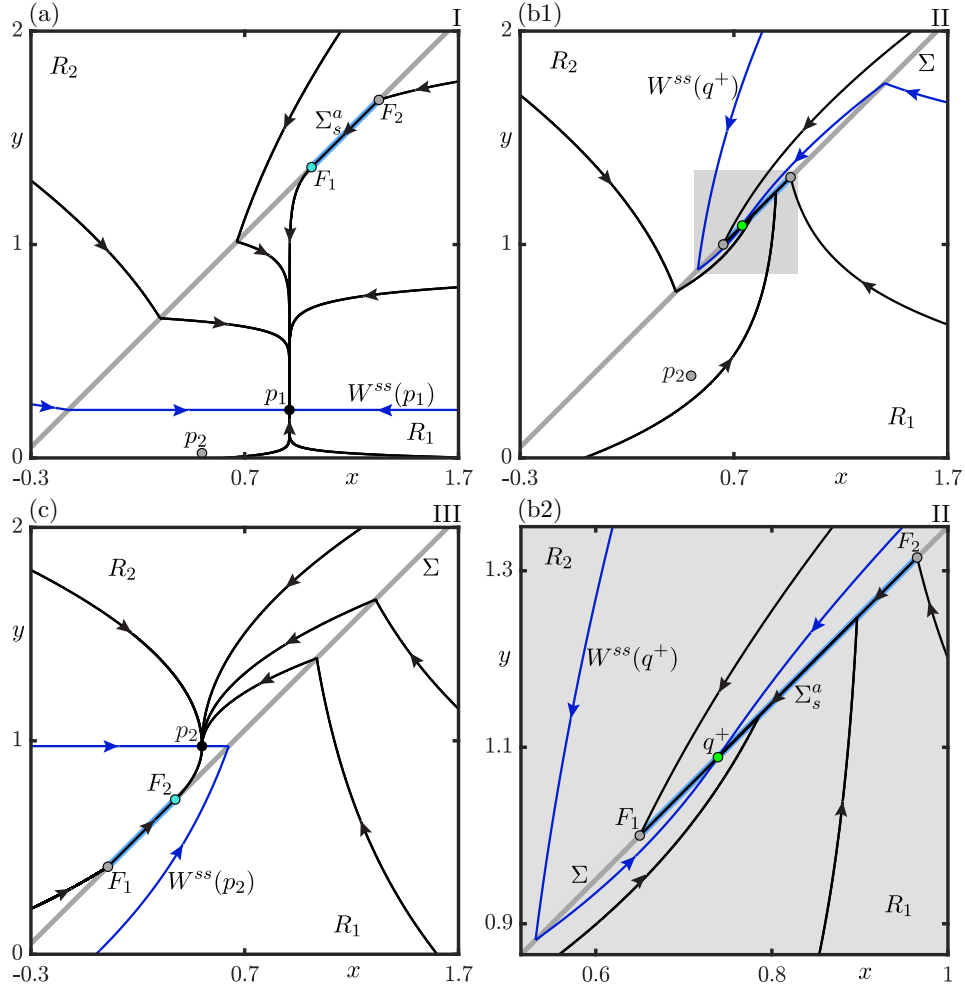


Figure 4: Representative phase portraits in regions I to III along the horizontal slice $\eta = 0.35$ of the (μ, η) -plane, each with an attracting sliding segment Σ_s^a bounded by quadratic tangency points F_1 and F_2 . Panel (a) for $\mu = 0.0225$ shows the admissible equilibrium p_1 with its strong stable manifold $W^{ss}(p_1)$, as well as the non-admissible equilibrium $p_2 \in R_1$. Panel (b1) for $\mu = 0.385$ and magnification (b2) near the sliding segment show $p_2 \in R_1$ and the attracting pseudo-node q^+ with strong stable manifold $W^{ss}(q^+)$. Panel (c) for $\mu = 0.975$ shows the admissible equilibrium $p_2 \in R_2$ with $W^{ss}(p_2)$.

in the pseudo-equilibrium q^+ being admissible. However, $q^+ \in \Sigma_s^r$ is now a repelling node with strong unstable manifold $W^{uu}(q^+)$, consisting of the departing orbits from q^+ in R_1 and R_2 , respectively. Importantly, in region V there is a stable (crossing) periodic orbit Γ , which is composed of orbit segments of f_1 in R_1 and f_2 in R_2 that join on the crossing segment Σ_c . All points except q^+ converge to this periodic orbit; in particular, $W^{uu}(q^+)$ accumulates on Γ , while initial conditions on $\Sigma_s^r \setminus \{q^+\}$ move to an end point F_2 or F_1 of Σ_s^r , where they depart into R_1 or R_2 , respectively, to converge to Γ ; see panel (b2). Crossing segment $\widehat{\text{BE}}_2^P$ concerns a second (persistence) boundary equilibrium bifurcation, but now of p_2 at the tangent point F_2 . As a result, the now admissible equilibrium p_2 is indeed the global attractor in region VI, as is shown in Figure 5(c).

Phase portraits for regions VII and VIII are presented in Figure 6; they both still feature the

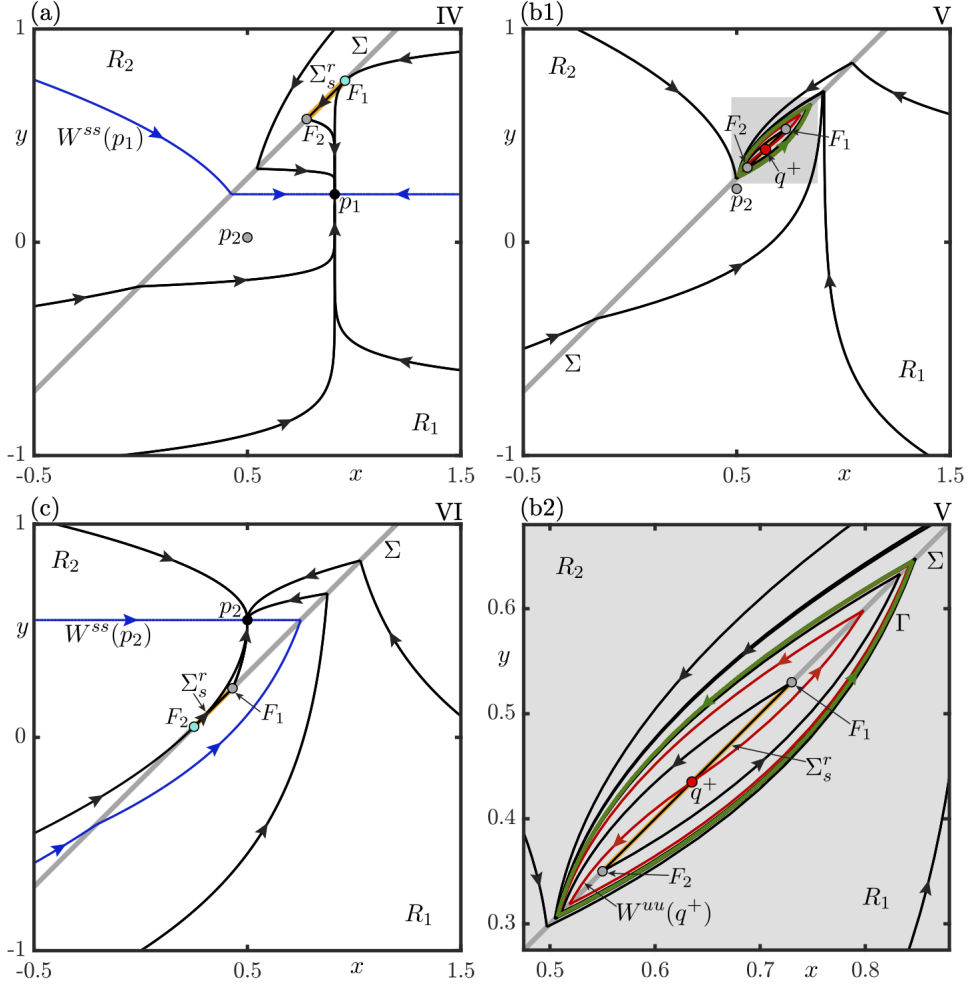


Figure 5: Representative phase portraits in regions IV to VI along a horizontal slice $\eta = -0.2$ of the (μ, η) -plane, each with a repelling sliding segment Σ_s^r bounded by quadratic tangency points F_1 and F_2 . Panel (a) for $\mu = 0.0225$ is similar to Figure 4(a), but now the sliding segment is repelling. Panel (b1) for $\mu = 0.25$ and the magnification near the sliding segment (b2) features a repelling pseudo-node q^+ with a strong unstable manifold $W^{uu}(q^+)$ and a (crossing) periodic orbit Γ that encircles Σ_s^r . Panel (c) for $\mu = 0.525$ is similar to Figure 4(c), but now the sliding segment is repelling.

repelling sliding segment Σ_s^r , bounded by the quadratic tangency points F_2 on the left and F_1 on the right. In region VII, as in panel (a1) with a magnification in panel (a2), we find the repelling pseudo-equilibrium $q^+ \in \Sigma_s^r$ as in region V. However, due to the transition through the bounding segment $\widetilde{\text{BE}}_2^F$ of (non-smooth fold) boundary equilibrium bifurcation, the equilibrium p_2 is now in open region R_2 and admissible, and the second pseudo-equilibrium q^- now also lies on Σ_s^r . The point p_2 attracts all points, apart from those on the generalised stable manifold $W_g^s(q^-)$ of q^- , which is composed of sliding orbits on Σ_s^r approaching q^- and the arriving orbit to F_2 . The unstable manifold $W^u(q^-)$ of q^- and strong unstable manifold $W^{uu}(q^+)$ both converge to the attractor p_2 . Note that $W^{ss}(p_2)$ is composed of a horizontal component in R_1 , the corresponding sliding orbit in Σ_s^r and the arriving orbit to F_1 . When crossing segment $\widetilde{\text{BE}}_1^P$ into region VIII, there is a (persistence) boundary equilibrium bifurcation, at which p_1 becomes admissible and the pseudo-equilibrium q^+ becomes non-admissible

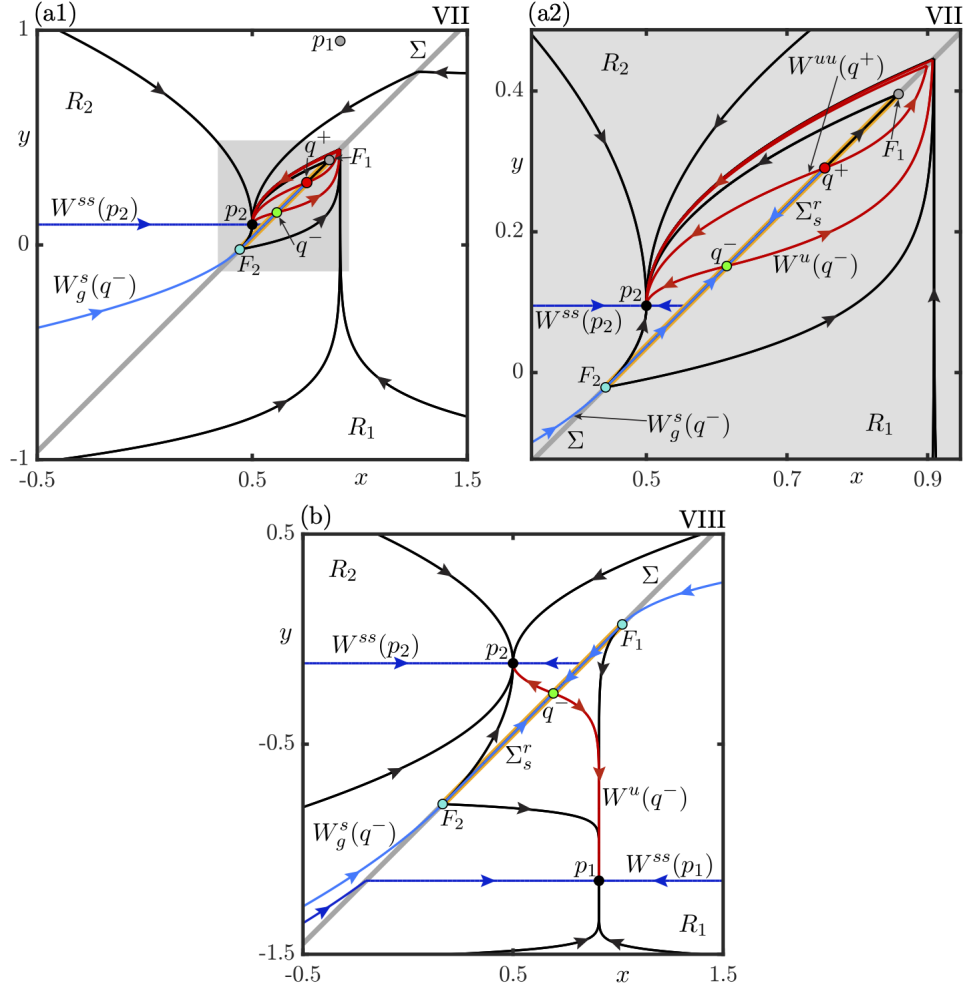


Figure 6: Representative phase portraits in regions VII and VIII, both with a repelling sliding segment Σ_s^r bounded by quadratic tangency points F_1 and F_2 . Panel (a1) for $(\mu, \eta) = (0.0987, -0.463)$ and the magnification near the sliding segment (a2) show p_2 with $W^{ss}(p_2)$, pseudo-saddle-equilibrium q^- with a generalised stable manifold $W_g^s(q^-)$ and unstable manifold $W^u(q^-)$, and the repelling pseudo-node q^+ with strong unstable manifold $W^{uu}(q^+)$. Panel (b) for $(\mu, \eta) = (-0.115, -0.95)$ shows the simultaneously admissible equilibria p_1 with $W^{ss}(p_1)$ and p_2 with $W^{ss}(p_2)$, and the pseudo-saddle-equilibrium q^- with $W_g^s(q^-)$ and $W^u(q^-)$.

by moving through F_1 onto the crossing segment Σ_c . As the phase portrait in Figure 6(b) shows, both $p_1 \in R_1$ and equilibrium $p_2 \in R_2$ are now attractors in region VIII; hence, this is the region of bistability. The generalised stable manifold $W_g^s(q^-)$ of the saddle pseudo-equilibrium $q^- \in \Sigma_s^r$ is now composed of Σ_s^r and the arriving orbits to both F_1 and F_2 , and it forms the boundary between the basins of attraction of the attractors p_1 and p_2 . Indeed, the lower branch of $W^u(q^-)$ converges to p_1 , and its upper branch to p_2 .

2.3 Codimension-one and codimension-two bifurcations

We now present analytical expressions for all (non-smooth) bifurcations of system (8) of codimension one and two in Propositions 3 and 4, respectively. The respective proofs can be found in Appendix A.

Proposition 3 (Codimension-one bifurcations). *System (8) has the following codimension-one bifurcations, further information on which can be found in [31].*

1. Boundary equilibrium bifurcations of p_1 and p_2 occur, respectively, along the straight lines

$$\begin{aligned} \text{BE}_1 : (\mu, \eta) &= \left(\mu, \frac{\mu}{\kappa_1} - \frac{1}{1 + \kappa_1} \right), \\ \text{BE}_2 : (\mu, \eta) &= \left(\mu, \frac{\mu}{\kappa_2} - \frac{1}{1 + \kappa_2} \right). \end{aligned}$$

At BE_i the equilibrium p_i collides with the tangency point F_i , changing its visibility. The tangency point F_1 is visible in regions I, IV and VIII. Similarly, the tangency point F_2 is visible in regions III, VI, VII and VIII. The pseudo-equilibrium q^+ is admissible in regions II, V and VII. Similarly, the pseudo-equilibrium q^- is admissible in regions VII and VIII.

2. Fold-fold bifurcations occur along the horizontal line

$$\text{FF} : (\mu, \eta) = (\mu, 0).$$

At FF the tangency points F_1 and F_2 coincide at a singular tangency point F^* and switch places on the sliding segment boundary, resulting in the sliding segments changing between being attracting and repelling [31]; see also Proposition 1 for a description of the tangency points.

3. A pseudo-saddle-node bifurcation occurs along the curve segment

$$\text{PS} : (\mu, \eta) = \left(\mu, -(\mu + 1) + 2\sqrt{\mu} \right), \quad \frac{\kappa_1^2}{(\kappa_1 + 1)^2} < \mu < \frac{\kappa_2^2}{(\kappa_2 + 1)^2}.$$

Along PS the pseudo-equilibria q^- and q^+ form a saddle-node at

$$q^* = (1 - \sqrt{\mu}) \begin{pmatrix} 1 \\ 1 \end{pmatrix} + \begin{pmatrix} 0 \\ \eta \end{pmatrix}$$

on the repelling sliding segment Σ_s^r .

The curves BE_1 , BE_2 , FF and PS from Proposition 3 intersect or meet at codimension-two bifurcation points. These points divide BE_1 , BE_2 , FF into the segments shown in Figure 3, along which the respective codimension-one bifurcation manifests itself in a topologically different way, as follows.

Proposition 4 (Codimension-two bifurcations). *System (8) has the following codimension-two bifurcations for $0 < \kappa_1 < \kappa_2$.*

1. Fold-boundary equilibrium bifurcations

$$\text{FB}_1 : (\mu, \eta) = \left(\frac{\kappa_1}{1 + \kappa_1}, 0 \right), \tag{24}$$

$$\text{FB}_2 : (\mu, \eta) = \left(\frac{\kappa_2}{1 + \kappa_2}, 0 \right), \tag{25}$$

occur at the intersection point of the curve FF with the curves BE₁ and BE₂, respectively. At the point FB_i, the equilibrium p_i collides with the singular tangency point F*.

The point FB_i divides the curve FF locally into segments FF₁ and FF₂, which is the case of fold-fold bifurcation of type VI₁ as presented in [31], and the segment FU of fused-focus bifurcation [31, 33] along which the (crossing) periodic orbit Γ (dis)appears. Both of these fold-fold bifurcations result in the sliding segment changing between being repelling and attracting, and the quadratic tangency points F_i switching places as the sliding segment boundaries.

The point FB_i also divides the curve BE_i locally into segment BE_i^P, where there is a standard persistence boundary equilibrium bifurcation with a nodal equilibrium as presented in [31], and a segment $\widehat{\text{BE}}_i^P$ along which a stable (crossing) periodic orbit Γ (dis)appears in a homoclinic-like persistence boundary equilibrium bifurcation.

2. A double-boundary equilibrium bifurcation

$$\text{BB} : (\mu, \eta) = \left(\frac{\kappa_1 \kappa_2}{(\kappa_1 + 1)(\kappa_2 + 1)}, \frac{-1}{(\kappa_1 + 1)(\kappa_2 + 1)} \right), \quad (26)$$

occurs at the intersection of the curves BE₁ and BE₂. At point BB the equilibria p₁, and p₂ simultaneously collide at the two different quadratic tangency points F₁ and F₂, respectively.

The point BB divides the curve BE₁ locally into segment $\widehat{\text{BE}}_1^P$, along which a stable (crossing) periodic orbit Γ (dis)appears, and a segment $\widetilde{\text{BE}}_1^P$, where there is a standard persistence boundary equilibrium bifurcation with a nodal equilibrium as presented in [31]. Similarly, the curve BE₂ is divided locally by BB into the segment $\widehat{\text{BE}}_2^F$, along which the (crossing) periodic orbit Γ (dis)appears, and a segment BE₂^F, where there is the standard non-smooth fold boundary equilibrium bifurcation with a nodal equilibrium [31].

3. Generalized boundary equilibrium bifurcations [30]

$$\text{GB}_1 : (\mu, \eta) = \left(\frac{\kappa_1^2}{(\kappa_1 + 1)^2}, -\frac{1}{(\kappa_1 + 1)^2} \right), \quad (27)$$

$$\text{GB}_2 : (\mu, \eta) = \left(\frac{\kappa_2^2}{(\kappa_2 + 1)^2}, -\frac{1}{(\kappa_2 + 1)^2} \right), \quad (28)$$

occur at end points of the curve PS, respectively, on the curves BE₁ and BE₂. At the point GB_i, equilibrium p_i collides with the quadratic tangency point F_i. At the same time, a pseudo-saddle-node bifurcation takes place at F_i, resulting in a generalised boundary equilibrium bifurcation with respect to f_i.

The point GB₁ separates the curve BE₁ locally into the segment $\widetilde{\text{BE}}_1^P$ and the segment BE₁^F of boundary equilibrium bifurcations. Similarly, the point GB₂ separates the curve BE₂ locally into the segment $\widehat{\text{BE}}_2^P$ and the segment $\widehat{\text{BE}}_2^F$ of boundary equilibrium bifurcations.

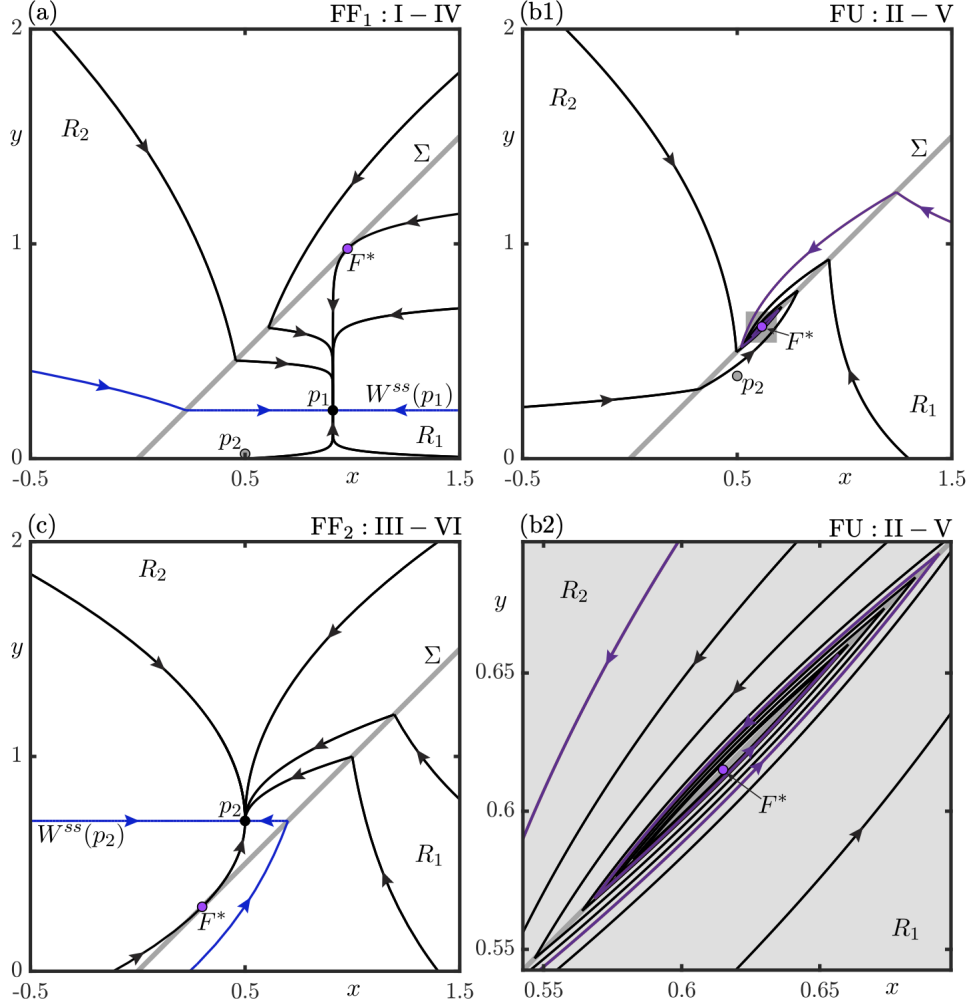


Figure 7: Representative phase portraits of segments FF_1, FU and FF_2 along $\eta = 0$, each with a singular tangency point F^* . Panel (a) for $\mu = 0.0225$ on FF_1 shows the global attractor p_1 with $W^{ss}(p_1)$ and the equilibrium p_2 . Panel (b1) for $\mu = 0.25$ on FU and the magnification (b2) shows the weakly attracting fold-fold point F^* ; a representative orbit is highlighted in purple. Panel (c) for $\mu = 0.7$ on FF_2 shows the global attractor p_2 with $W^{ss}(p_2)$.

2.4 Phase portraits at codimension-one bifurcations

We now present in Figures 7–11 phase portraits in the (x, y) -plane for each segment of codimension-one bifurcation introduced in Proposition 4 and shown and labeled accordingly in Figure 3. Here, we take a global view of each such transition to allow for comparison with the respective neighbouring structurally stable phase portraits in Figures 4–6.

2.4.1 Fold-fold and pseudo-Hopf bifurcations

Figure 7 shows the phase portraits along segments FF_1, FU , and FF_2 , each of which with a singular tangency point F^* . The phase portrait along segment FF_1 , which separates regions I and IV, is shown in panel (a). The admissible equilibrium $p_1 \in R_1$ is a global attractor with strong stable manifold $W^{ss}(p_1)$. The singular tangency at the point F^* is invisible to f_2 and visible to f_1 , and orbits of

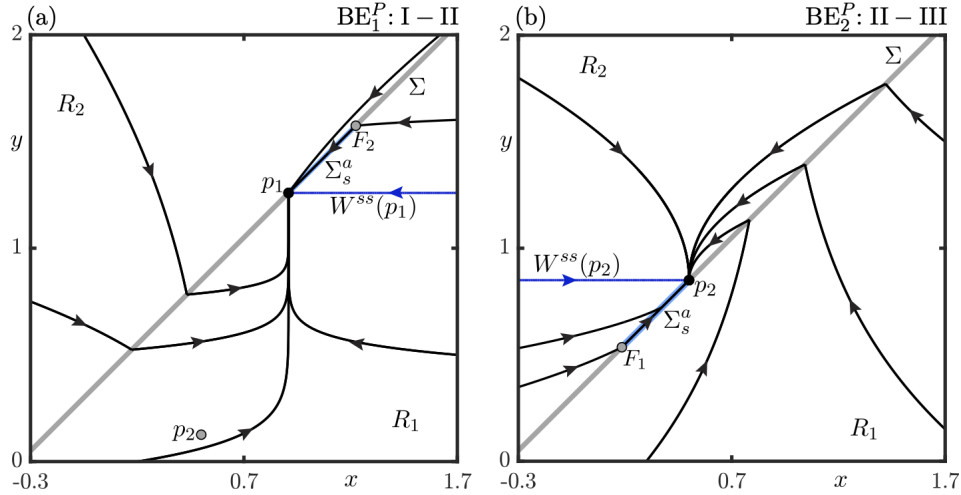


Figure 8: Representative phase portraits along the segments BE_1^P and BE_2^P on the horizontal slice $\eta = 0.35$ of the (μ, η) -plane, each with an attracting sliding segment Σ_s^a . Panel (a) for $\mu = 0.1259$ on BE_1^P shows boundary equilibrium p_1 with $W^{ss}(p_1)$. Panel (b) for $\mu = -0.25$ on BE_2^P shows the boundary equilibrium p_2 with $W^{ss}(p_2)$.

system (8) are collinear at F^* . The phase portrait along segment FU, separating regions II and V, is shown in panel (b1) with a magnification near F^* in panel (b2). The singular tangency at F^* is now invisible to both vector fields f_1 and f_2 , and orbits are anti-collinear at F^* . Therefore, orbits spiral inward toward F^* (at a very slow rate), and this point is a global attractor. This situation is reminiscent of a (supercritical) Hopf bifurcation for smooth dynamical systems, which is why this bifurcation is also known as a pseudo-Hopf bifurcation [33]. The phase portrait along segment FF_2 , which separates regions III and VI, is presented in panel (c). The singular tangency at F^* is now visible to f_2 and invisible to f_1 , and $p_2 \in R_2$ is admissible and the global attractor.

2.4.2 Boundary equilibrium and pseudo-saddle-node bifurcations

The phase portraits along the segments of the curves BE_1 and BE_2 from Proposition 3 are characterised by an equilibrium of system (8) being on the switching manifold, but they have different global manifestations.

The phase portrait along segment BE_1^P , which separates regions I via II, is shown in Figure 8(a). It has the attracting sliding segment Σ_s^a bounded by the boundary-node p_1 on the left, and by the invisible quadratic tangency point F_2 on the right; both pseudo-equilibria q^- and q^+ are non-admissible (and not shown). The equilibrium p_2 is not admissible and the boundary-node p_1 is a global attractor; note that its strong stable manifold $W^{ss}(p_1)$ consists only of the horizontal arriving orbit to p_1 in R_1 . The phase portrait in panel (b) along segment BE_2^P , separating regions II and III, is the corresponding situation but for the boundary-node p_2 : this point is now the global attractor with strong stable manifold $W^{ss}(p_2)$ in R_2 , and it bounds Σ_s^a together with the invisible quadratic tangency point F_1 .

Figure 9(a1) shows the phase portrait along segment \widehat{BE}_1^P , separating regions IV and V, with a magnification in panel (a2) near the sliding segment, which is now repelling. Here Σ_s^r is bounded by the invisible quadratic tangency point F_2 on the left and by the boundary-node p_1 on the right, with both pseudo-equilibria non-admissible (and not shown). The point p_1 is globally attracting with strong stable manifold $W^{ss}(p_1)$ in R_1 . However, the vector field f_2 is transverse to Σ at p_1 , and this

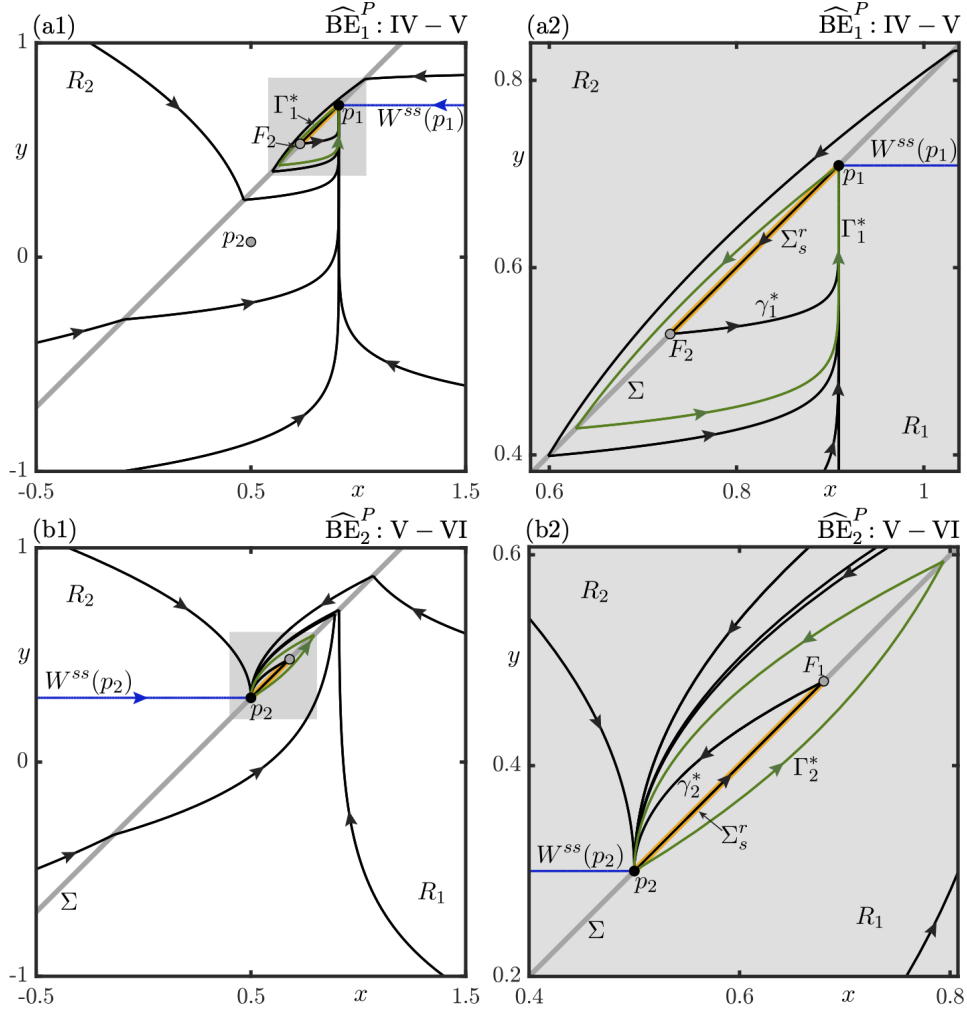


Figure 9: Representative phase portraits along segments $\widehat{\text{BE}}_1^P$ and $\widehat{\text{BE}}_2^P$ on the horizontal slice $\eta = -0.2$ in the (μ, η) -plane, each with a repelling sliding segment Σ_s^r . Panel (a1) for $\mu = 0.0709$ on $\widehat{\text{BE}}_1^P$ and the magnification (a2) show the boundary equilibrium p_1 with $W^{ss}(p_1)$, and homoclinic connections γ_1^* and Γ_1^* . Panel (b1) for $\mu = 0.3$ on $\widehat{\text{BE}}_2^P$ and the magnification (b2) show boundary equilibrium p_2 with $W^{ss}(p_2)$, and homoclinic connections γ_2^* and Γ_2^* .

departing orbit forms a non-sliding homoclinic connection Γ_1^* back to the boundary-node p_1 . Observe in panel (a2) that Γ_1^* bounds a region of a family of homoclinic orbits that involve sliding (in backward time) along the repelling sliding segment Σ_s^r . The orbit labeled γ_1^* , consisting of Σ_s^r and the departing orbit from F_2 , is the maximal sliding homoclinic orbit: it divides this region inside Γ_1^* into homoclinic orbit that remain in R_1 from those that have segments in both R_1 and R_2 . The phase portrait along segment $\widehat{\text{BE}}_2^P$, which separates regions V and VI, is shown similarly in Figure 9(b1) and (b2). The overall picture is effectively that same, but now p_2 is the globally attracting boundary equilibrium on Σ_s^r , with analogous non-sliding and maximal sliding homoclinic orbits Γ_2^* and γ_2^* , respectively. The characterising feature of this bifurcation is the existence of a non-sliding and crossing homoclinic connection Γ_i^* , from which the stable (crossing) periodic orbit Γ in region V bifurcates; compare with Figure 5(b). This type of (persistence) boundary equilibrium bifurcation is hardly discussed in the

literature; to our knowledge, it has only been observed in the related Welander's box model in [24], where it is referred to as a homoclinic-like boundary equilibrium bifurcation.

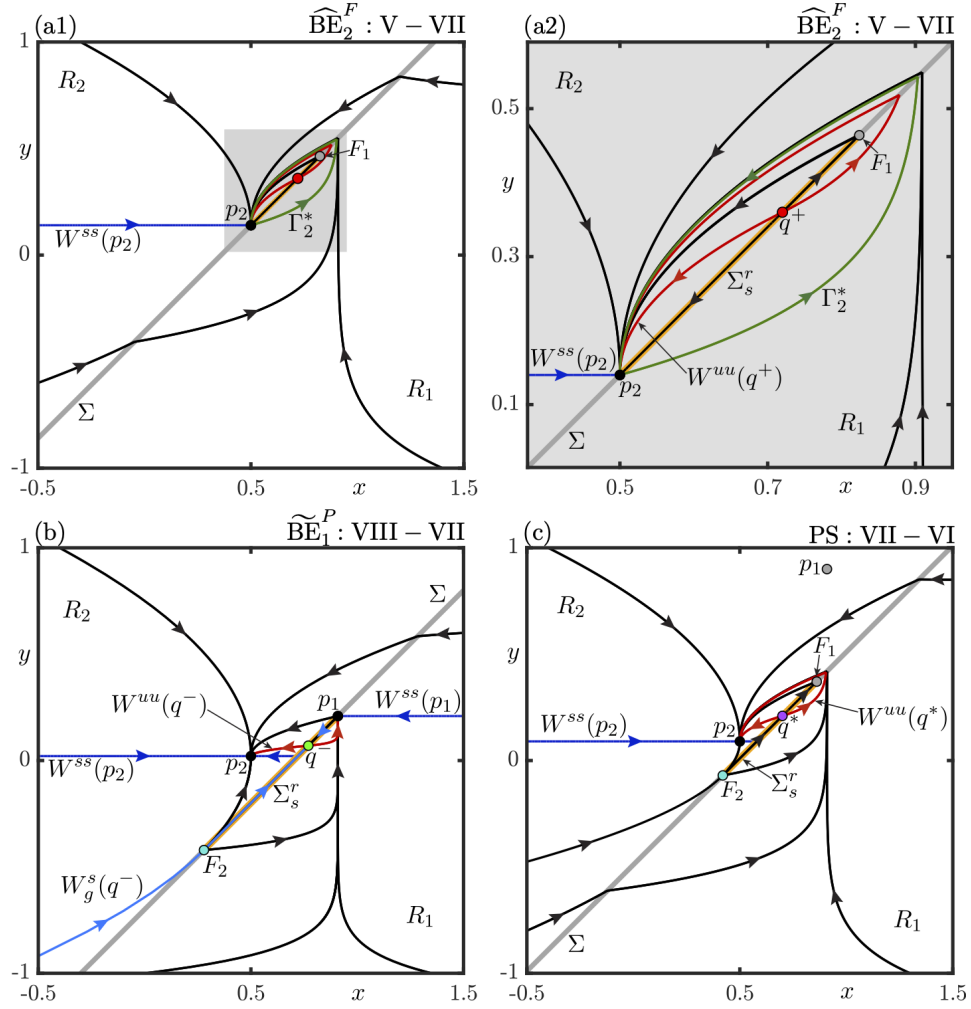


Figure 10: Representative phase portraits along segments $\widehat{\text{BE}}_2^F$, $\widetilde{\text{BE}}_1^P$ and along the curve PS, each with a repelling sliding Σ_s^a . Panel (a1) for $(\mu, \eta) = (0.14, -0.36)$ on $\widehat{\text{BE}}_2^F$ and the magnification (a2) show the boundary equilibrium p_2 with $W^{ss}(p_2)$ and homoclinic connection Γ_2^* , and the pseudo-equilibrium q^+ with $W^{uu}(q^+)$. Panel (b) for $(\mu, \eta) = (-0.0141, -1.05)$ on $\widetilde{\text{BE}}_1^P$ shows the admissible equilibrium $p_2 \in R_2$ with $W^{ss}(p_2)$, the boundary equilibrium p_1 with $W^{ss}(p_1)$, and the pseudo-equilibrium q^- with $W^u(q^-)$ and $W_g^s(q^-)$. Panel (c) for $(\mu, \eta) = (0.09, -0.7636)$ on PS shows the equilibrium p_2 with $W^{ss}(p_2)$ and the singular pseudo-equilibrium q^* with $W^{uu}(q^*)$.

The phase portrait along segment $\widehat{\text{BE}}_2^F$, which separates regions V and VII, is shown in Figure 10(a1) with a magnification near the repelling sliding segment in panel (a2). Here, Σ_s^r is bounded by the attracting boundary-node p_2 on the left and by an invisible tangency F_1 on the right; moreover, it contains the admissible and repelling pseudo-equilibrium $q^+ \in \Sigma_s^r$ (while the pseudo-equilibrium q^- is non-admissible and not shown). As was the case along segment $\widehat{\text{BE}}_1^F$, the phase portrait in Figure 10(a) features a (crossing) homoclinic orbit Γ_2^* of p_2 . However, due to the existence of q^+ on Σ_s^r , this special orbit does now not bound a region with further (sliding) homoclinic orbits. Regardless,

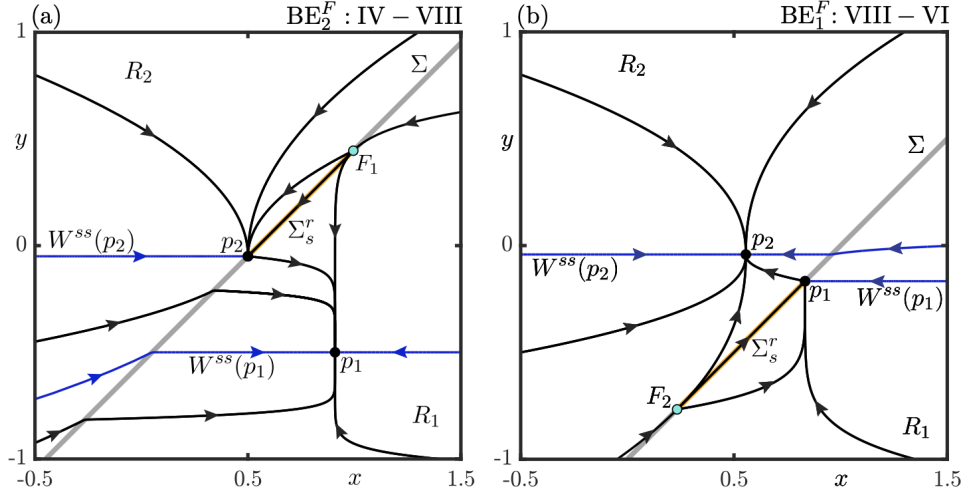


Figure 11: Representative phase portraits along the segments BE_2^F and BE_1^F , each with a repelling sliding segment Σ_s^r . Panel (a) for $(\mu, \eta) = (-0.05, -0.55)$ on BE_2^F shows the boundary equilibrium p_2 with $W^{ss}(p_2)$ and the admissible equilibrium $p_1 \in R_1$ with $W^{ss}(p_1)$. Panel (b) for $(\mu, \eta) = (0.0209, -0.7)$ on BE_1^F similarly shows the boundary equilibrium p_1 with $W^{ss}(p_1)$ and the admissible equilibrium $p_2 \in R_2$ with $W^{ss}(p_2)$.

Γ_2^* is still the limit of the stable (crossing) periodic orbit Γ in region V. Note that all points inside the region bounded by Γ_2^* converge in backward time to the unstable pseudo-equilibrium q^+ , whose strong unstable manifold $W^{uu}(q^+)$ converges to p_2 ; see panel (a2). Segment \widetilde{BE}_1^P separates regions VII and VIII, and the phase portrait along it is shown in Figure 10(b). Here, p_1 is the attracting boundary-node, and the quadratic tangency F_2 is visible. The equilibrium $p_2 \in R_2$ is admissible and also attracting. Moreover, the pseudo-equilibrium q^- lies on the repelling sliding section Σ_s^r , and it is a saddle. Its generalised stable manifold $W_g^s(q^-)$ consists of Σ_s^r and the arriving orbit to F_2 . The boundary between the basins of attraction of p_1 and p_2 is formed by the union of $W_g^s(q^-)$ and the strong stable manifold $W^{ss}(p_1)$ in R_1 . Points below these curves and including $W^{ss}(p_1)$ converge to p_1 , while points above these curves converge to p_2 .

The pseudo-saddle-node bifurcation along the curve PS separates regions VI and VII, and its phase portrait is shown in Figure 10(c). As the name suggests, there is a saddle-node q^* of pseudo-equilibria on the repelling sliding segment Σ_s^r , which is the limiting point where the admissible pseudo-equilibria $q^-, q^+ \in \Sigma_s^r$ in region VII (dis)appear. Note that q^* is semi-stable on Σ_s^r and has the strong unstable manifold $W^{uu}(q^*)$. The points on Σ_s^r in between the visible quadratic tangency point F_2 and q^* end up at q^* under the sliding flow; all other points in the (x, y) -plane converge to the admissible and stable equilibrium $p_2 \in R_2$ with strong stable manifold $W^{ss}(p_2)$.

Finally, the boundary equilibrium bifurcations along segments BE_2^F and BE_1^F are encountered in the transition from region IV via region VIII to region VI. In the phase portrait for BE_2^F in Figure 11(a), the attracting boundary-node p_2 bounds the repelling sliding segment Σ_s^r on the left, while a visible quadratic tangency point F_1 bounds it on the right. There are no pseudo-equilibria on Σ_s^r , and the equilibrium $p_1 \in R_1$ is admissible and also attracting. Trajectories above and including the union of $W^{ss}(p_2)$ in R_2 , Σ_s^r and the arriving orbit to F_1 in R_1 converge to p_2 , and orbits below this union converge to p_1 . The phase portrait along segments BE_1^F in Figure 11(b) is effectively the same with the roles of p_1 and p_2 exchanged. Here, the orbits below and including the union of the

arriving orbit to F_2 in R_2 , Σ_s^r and $W^{ss}(p_1)$ in R_1 converge to the attracting boundary node $p_1 \in \Sigma_s^r$, while orbits above this union converge to the attracting equilibrium $p_2 \in R_2$.

3 Bifurcation analysis of the smooth model

We now investigate the smooth model (7) for small $\varepsilon > 0$. Here we again fix the vertical mixing coefficients to $\kappa_1 = 0.1$ and $\kappa_2 = 1.0$, to enable a direct comparison of the bifurcation diagram of system (7) with that of the limiting case of system (8).

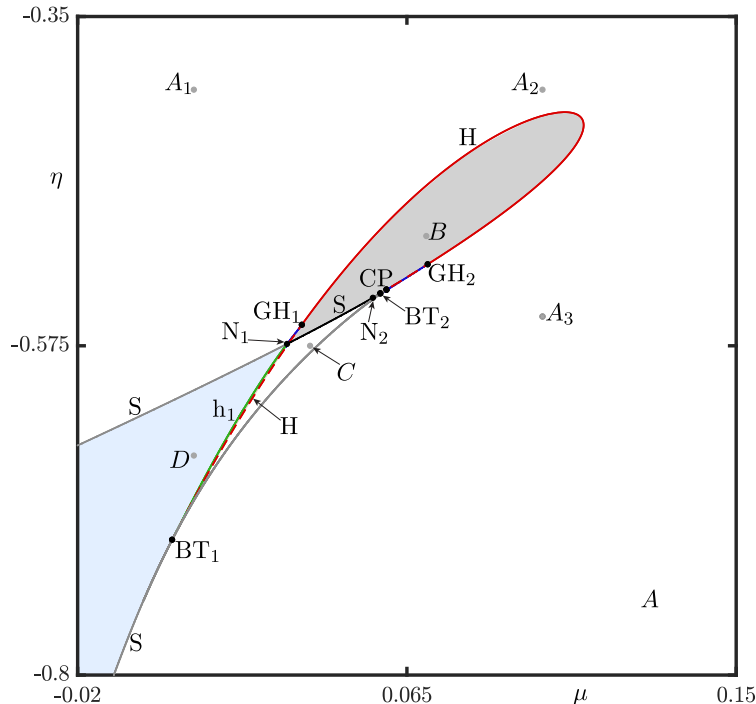


Figure 12: Two-parameter bifurcation diagram in the (μ, η) -plane of system (7) for $\varepsilon = 0.1$ and with $\kappa_1 = 0.1$, $\kappa_2 = 1.0$. Shown are curves of Hopf bifurcation H (red, solid when supercritical, dashed when subcritical), saddle-node bifurcation S (black when on periodic orbit and grey otherwise) and homoclinic bifurcation h_1 (green), which are the main curves that divide the (μ, η) -plane into the large regions A, B, C and D . Also shown are codimension-two points CP, BT₁, BT₂, GH₁, GH₂, N₁ and N₂; grey shading indicates the existence of a stable periodic orbit, and blue shading bistability between equilibria.

We first consider the bifurcation diagram in the (μ, η) -plane of system (7) for the fixed value of $\varepsilon = 0.1$. It is shown in Figure 12 and was obtained by computing the shown bifurcation curves and codimension-two points with the continuation package AUTO-07p [27], guided by established bifurcation theory [26]. One clearly observes four main open regions, denoted A, B, C and D , on which we focus here; associated phase portraits are shown in Figures 13–15.

A main element of the bifurcation diagram in Figure 12 is a curve S of saddle-node bifurcation with two branches that meet at the cusp point CP. Along each branch of S there are points BT₁ and BT₂ of Bogdanov-Takens bifurcation (one close to CP). From these points a curve H of Hopf bifurcation emerges, which is the second main element of the bifurcation diagram. Together, the

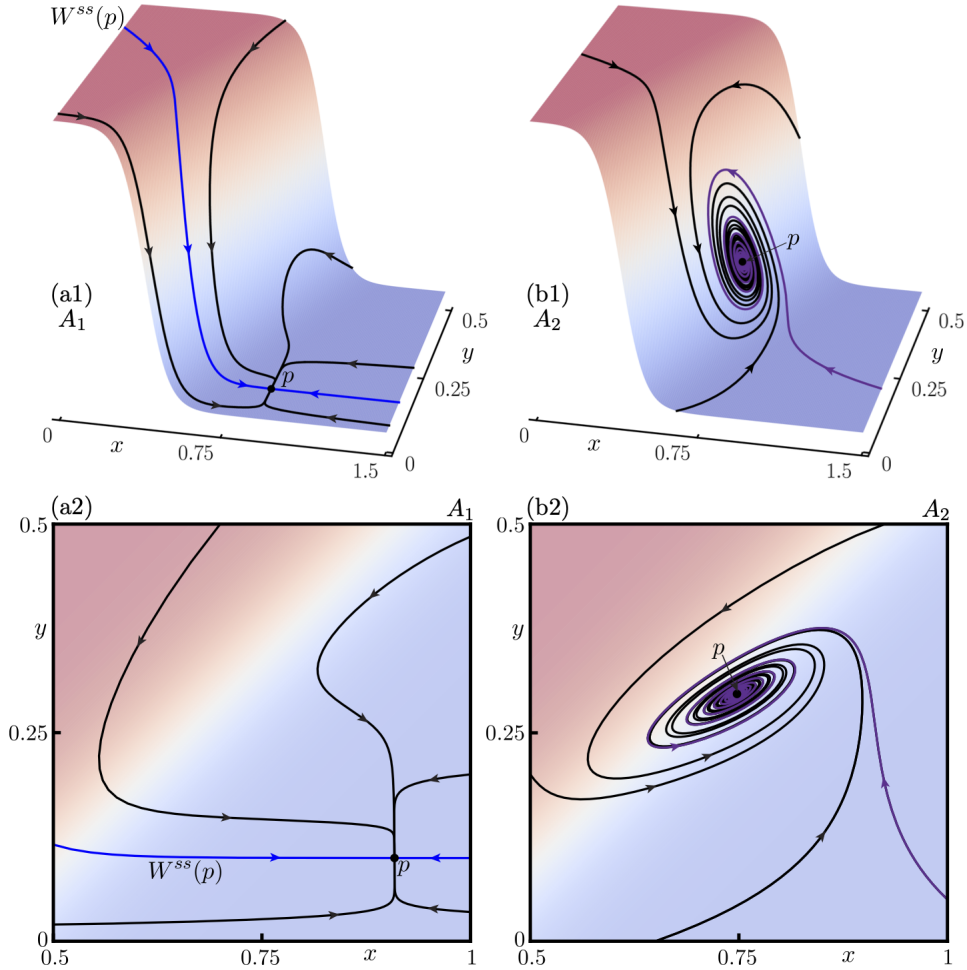


Figure 13: Phase portraits at the points A_1 at $\mu = 0.01$ and A_2 at $\mu = 0.1$ with $\eta = -0.4$ from region A in Figure 12. Panels (a1) and (b1) shows the phase portrait on the graph of $\mathcal{H}_{0.1}(x, y)$, and panels (a2) and (b2) in the (x, y) -plane. Featured is the equilibrium p , its strong stable manifold $W^{ss}(p)$ (blue curve) when it exists, and some representative trajectories (purple curves).

curves S and H effectively form the boundaries of the four main regions A , B , C and D . Additional ingredients are: the change of criticality of H at generalised Hopf points GH_1 and GH_2 ; a curve h_1 of homoclinic bifurcation; and a segment of S , bounded by points N_1 and N_2 of non-central homoclinic bifurcation [34], where the saddle-node bifurcation occurs on a periodic orbit (also known as SNIC or SNIPER). We remark that the complete bifurcation diagram in the (μ, η) -plane involves subtle additional bifurcation phenomena near the points GH_1 , GH_2 , N_1 and N_2 that are indistinguishable on the scale of Figure 12; these include very narrow regions bounded by additional curves of homoclinic bifurcation and of saddle-node bifurcation of periodic orbits, and their discussion is beyond the scope of this paper.

3.1 Phase portraits in the main regions of the (μ, η) -plane

Region A of Figure 12 is bounded by the respective (supercritical) part of the curves S and H . Comparison with Figure 3 shows that A is the largest region and ‘covers’ the five regions I, II, III,

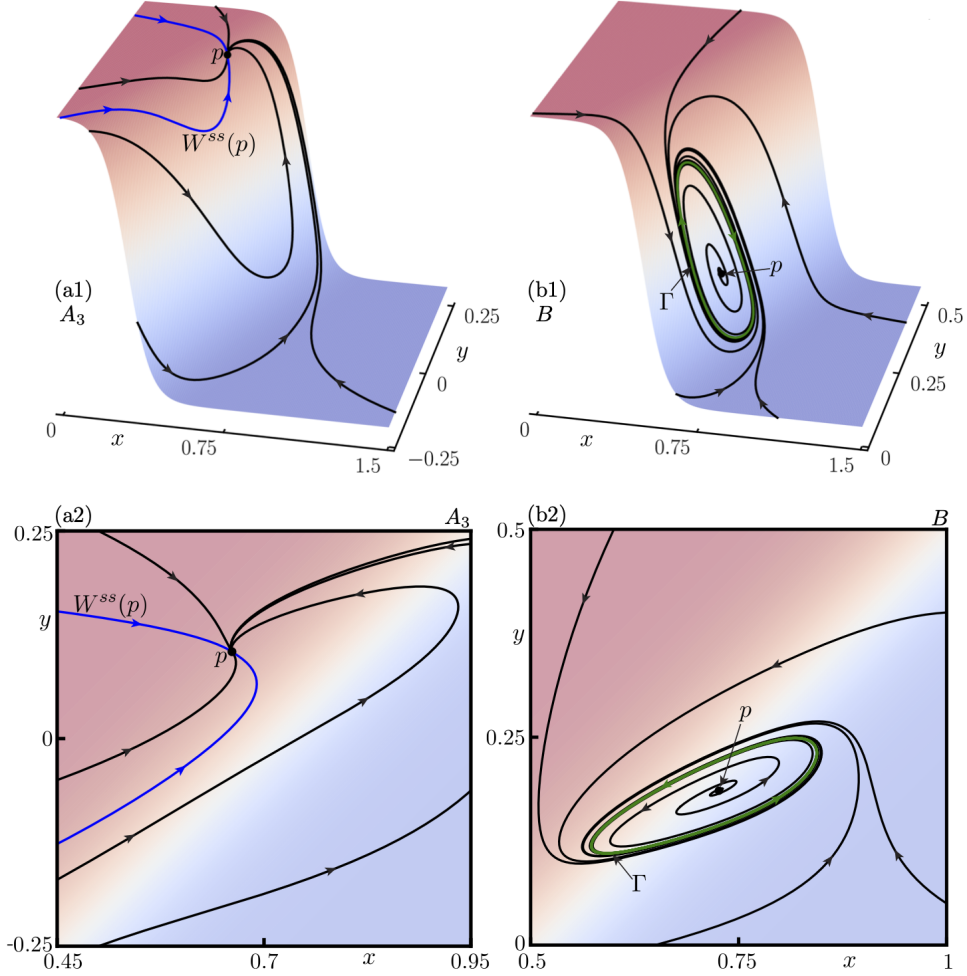


Figure 14: Phase portraits at the point A_3 at $(\mu, \eta) = (0.1, -0.555)$ and from region B at $(\mu, \eta) = (0.07, -0.50)$, shown as in Figure 13 and featuring a periodic orbit Γ in panels (b1) and (b2).

IV and VI of the PWS system (8). Throughout region A , there is a single attracting equilibrium, denoted p , which may correspond to distinct mixing states: weak (non-convective) mixing near κ_1 , an intermediate state in between convective and non-convective mixing, or strong (convective) mixing near κ_2 . This is illustrated in Figures 13 and 14(a) with phase portraits at the parameter points labeled A_1 , A_2 and A_3 in Figure 12. We show all phase portrait of system (7) in two ways to indicate when the dynamics corresponds to κ_1 or κ_2 : on the graph of $\mathcal{H}_\varepsilon(y-x-\eta)$ over the (x, y) -plane and on the (x, y) -plane itself, where we use coloring as in Figure 2. At parameter point A_1 as in Figure 13(a), the single stable equilibrium p lies in the region with $\mathcal{H}_{0.1}(y-x-\eta)$ near 0 (that is, the dynamics of system (7) is near κ_1), and it has real eigenvalues and a strong stable manifold $W^{ss}(p)$; hence, p corresponds here to the equilibrium $p_1 \in R_1$ from regions I and IV of the PWS system (8). Moving to parameter point A_2 as in Figure 13(b), the equilibrium p now lies in the transition region where the graph of $\mathcal{H}_{0.1}(y-x-\eta)$ is steep; moreover, it is an attracting focus with complex conjugate eigenvalues. Finally, at parameter point A_3 as in Figure 14(a), the attracting point p has again real eigenvalues and a strong stable manifold $W^{ss}(p)$, and now lies in the region of the phase plane with $\mathcal{H}_{0.1}(y-x-\eta)$ near 1 (that is, the dynamics is now near κ_2). Hence, p now corresponds to the equilibrium $p_2 \in R_2$

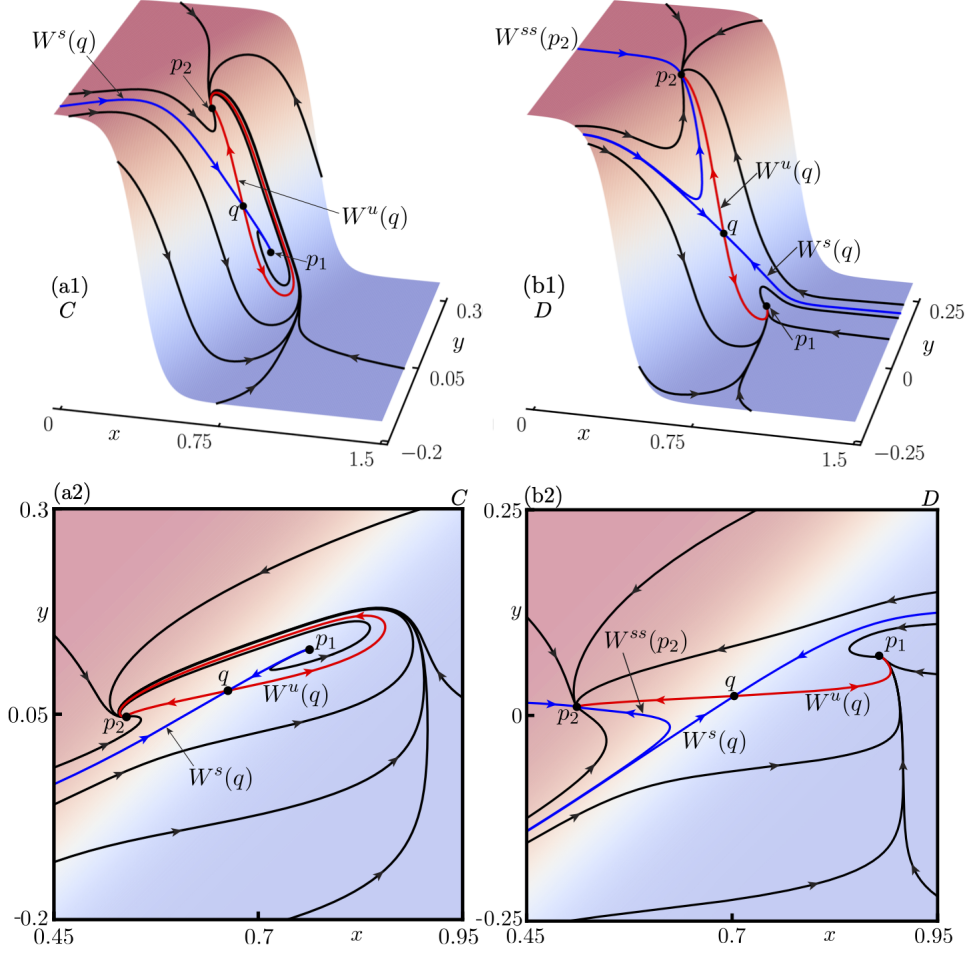


Figure 15: Phase portraits in the region C at $(\mu, \eta) = (0.04, -0.575)$ and region D at $(\mu, \eta) = (0.01, -0.65)$. Shown in the same manner as in Figure 13, now featuring equilibria p_1, p_3 , and q with the stable manifold $W^s(q)$ and unstable manifold $W^u(q)$.

in either regions III and VI of the PWS limit. We conclude that the gradual transition from A_1 to A_3 within region A is very reminiscent of that from region I, via region II, to region III of system (8); compare with Figure 4.

Region B is bounded by the supercritical part of the curve H and the SNIPER-part of S, and it is the ‘smooth version’ of region V of system (8). The phase portrait in Figure 14(b), at the marked parameter point in Figure 12, shows that in region B there is indeed a stable periodic orbit Γ surrounding the now unstable equilibrium p . Observe that Γ ‘lives’ in the switching region; that is, it lies on the steep part of the graph of $\mathcal{H}_{0,1}(y - x - \eta)$. Note further that the periodic orbit Γ bifurcates at the supercritical part of the Hopf bifurcation curve H from the attracting focus p of the phase portrait at A_2 in Figure 13(b). As η is decreased within region B , the periodic orbit Γ grows and develops two segments that lie in the region with $\mathcal{H}_{0,1}(y - x - \eta)$ near 0 and near 1, respectively; these segments correspond to the two segments of the segments periodic orbit Γ in V of the limiting PWS system (8) in Figure 5(b).

Region C of Figure 12 is bounded by segments of the two branches of S and by the homoclinic

bifurcation curve h_1 (which follows closely a subcritical part of the curve H). Figure 15(a) shows the representative phase portrait at the marked parameter point in Figure 12. There is an attracting equilibrium, labeled p_2 , with a high value of the transition function $\mathcal{H}_{0.1}$, as well as a saddle-equilibrium q and a repelling equilibrium p_1 with an intermediate value of $\mathcal{H}_{0.1}$. Note that q has the stable manifold $W^s(q)$ and unstable manifold $W^u(q)$, which converges to p_2 . Region C is the ‘smooth version’ of region VII of the limiting PWS system (8) in the following way: p_2 of the smooth system (7) corresponds to $p_2 \in R_2$, and the equilibria q and p_1 correspond to the pseudo-saddle-equilibrium q^- and pseudo-equilibrium q^+ on the repelling sliding segment Σ'_s , respectively; compare with Figure 6(a).

Finally, region D is bounded by the other segments of the two branches of S and the homoclinic bifurcation curve h_1 . As the representative phase portrait in Figure 15(b) at the marked parameter point in Figure 12 shows, it is the region of bistability and corresponds to region VIII of the system (8). The attractor p_2 in Figure 15(b) is still at a high value of $\mathcal{H}_{0.1}$, and the saddle-equilibrium q is unchanged. However, in contrast to region C , the equilibrium p_1 is at lower value of the transition function and, moreover, it is now an attractor. The lower branch of $W^u(q)$ converges to p_1 and its upper branch to p_2 , meaning that the stable manifold $W^s(q)$ forms the boundary between the basins of attraction of p_1 and p_2 ; compare with Figure 6(b).

3.2 Partial bifurcation analysis in (μ, η, ε) -space

We now describe how the main elements of the bifurcation diagram of system (7) in the (μ, η) -plane change with the switching-time parameter ε . Our focus here is on the curves S and H, which meet at the Bogdanov-Takens points BT_1 and BT_2 and effectively delimit the two main regions of interest, namely region B characterised by stable oscillations and region D exhibiting bistability. Figure 16 presents the partial three-parameter bifurcation diagram in (μ, η, ε) -space for $\varepsilon \in [0, 0.16]$ and ranges of μ and η as in Figure 3. Specifically, Figure 16 shows the bifurcation diagram of the limiting system (8) for $\varepsilon = 0$ together with the curves S and H of system (7) as computed for 31 equidistant slices of fixed $\varepsilon > 0$. In this way, the corresponding surfaces S and H of saddle-node and Hopf bifurcation are visualised in (μ, η, ε) -space with a ‘see-through effect’. Also shown in Figure 16 is the curve CP of cusp bifurcation, and the curves BT_1 and BT_2 of Bogdanov-Takens bifurcation, along which the surface H ends on the surface S. These codimension-two bifurcation curves were computed directly by numerical continuation in (μ, η, ε) -space. In particular, this shows that BT_1 and BT_2 form a single curve with a maximum at the point DBT at $\varepsilon \approx 0.147$, which we identified as a codimension-three degenerate Bogdanov-Takens point of focus type [35, 36]. Additionally, curves GH_1 and GH_2 of generalised Hopf bifurcation are shown in Figure 16; they were found by identifying the points the corresponding bifurcation points on the curves of Hopf bifurcation in the individual slices for fixed ε . We observe for increasing ε that the curve GH_1 ends at the point DBT. The curve GH_2 , on the other hand, terminates where the curves CP and BT_2 intersect at the codimension-three point GBC at $\varepsilon \approx 0.1208$. Similarly, the codimension-two non-central homoclinic bifurcation N_1 and N_2 (not shown in Figure 16) are found to vanish as ε increases, prior to ε reaching the value $\varepsilon \approx 0.147$ of the point DBT. The disappearance of N_1 and N_2 involves a sequence of codimension-three bifurcations, whose analysis is beyond the scope of this paper.

We first consider the relevance of the PWS limiting system (8) for the bifurcation diagram of the smooth system (7). While the continuation of Hopf and saddle-node bifurcation of system (7) becomes very challenging for small values of ε near 0, we managed to compute the respective curves S and H in the slice at $\varepsilon = 0.005$. As illustrated in Figure 16, this turns out to be sufficient for determining the convergence of S and H to the corresponding non-smooth bifurcation as ε approaches 0. Specifically, the lower boundary of the surface S of saddle-node bifurcation in the (μ, η) -plane at $\varepsilon = 0$ is the union

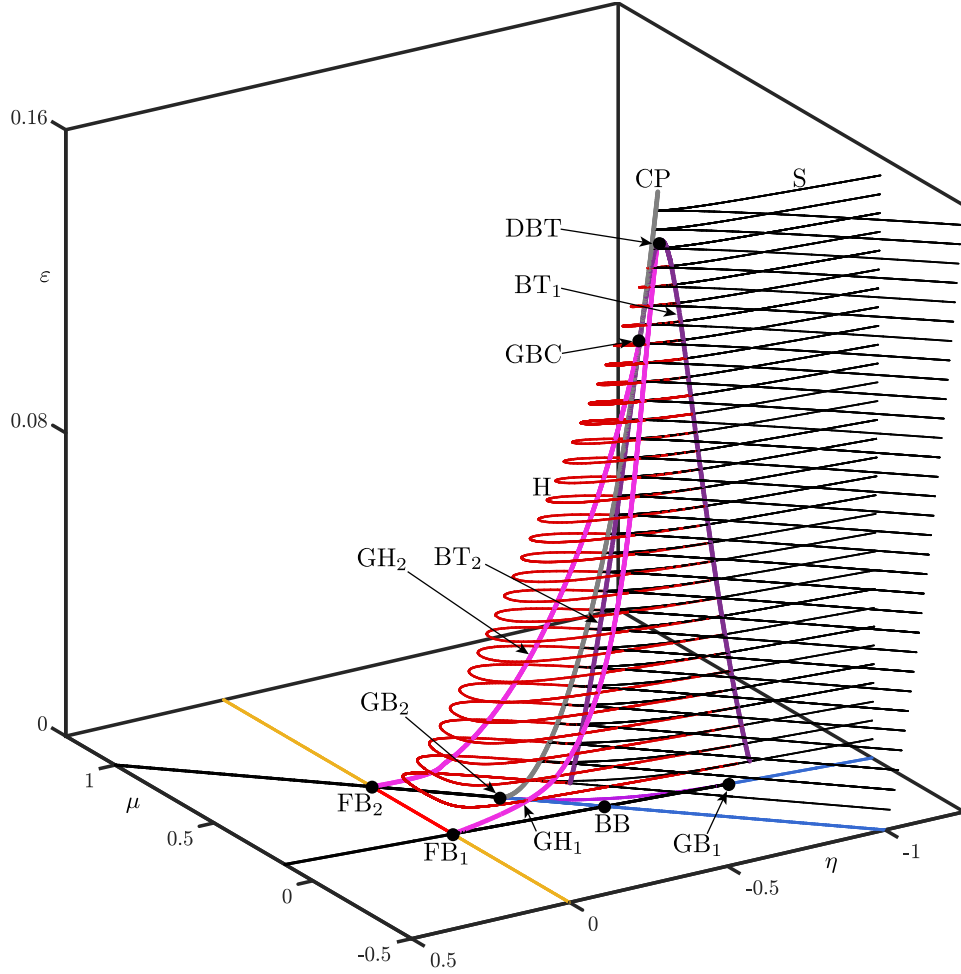


Figure 16: Partial three-parameter bifurcation diagram in (μ, η, ε) -space of system (7) for $\varepsilon > 0$ and system (8) at $\varepsilon = 0$, with $\kappa_1 = 0.1$ and $\kappa_2 = 0.1$. Represented are curves S of saddle-node bifurcation (black) and H of Hopf bifurcation (red) for fixed values of $\varepsilon > 0$, together with the bifurcation diagram for $\varepsilon = 0$ from Figure 3. The diagram also illustrates the curve CP of cusp bifurcation (grey), along with branches BT₁ and BT₂ of Bogdanov-Takens bifurcation (dark purple) that meet at the point DBT. Included are also curves GH₁ and GH₂ of generalised Hopf bifurcation (pink).

of the non-smooth fold boundary equilibrium bifurcation curve segments BE_1^F , BE_2^F and \widehat{BE}_2^F , and the pseudo-saddle-node bifurcation PS. The surface H of Hopf bifurcation has as its boundary at $\varepsilon = 0$ the union of the curve segments \widehat{BE}_1^P , \widehat{BE}_2^P and \widetilde{BE}_1^P of persistence boundary equilibrium bifurcation, and FU of fused-focus bifurcation. Moreover, the curves BT₁ and BT₂ of Bogdanov-Takens bifurcation converge to the points GB₁ and GB₂ of generalised boundary equilibrium bifurcation, respectively; the curve CP of cusp bifurcation also converges to the point GB₂. Similarly, the curves GH₁ and GH₂ of generalised Hopf bifurcation converge to the points FB₁ and FB₂ of fold-boundary equilibrium bifurcation, respectively.

We now consider the influence of increasing the switching-time parameter ε . Observe from Figure 16 that the surface H of Hopf bifurcation ‘ends’ at the point DBT at $\varepsilon \approx 0.147$. Specifically, the curve H in the (μ, η) -plane for fixed $\varepsilon < 0.147$ shrinks to a point at DBT and disappears. Since all

other curves of codimension-two bifurcations have also disappeared, above DBT one only finds the surface S of saddle-node bifurcation with the curve CP of cusp bifurcation. Therefore, in any slice for fixed $\varepsilon > 0.147$ the remaining regions are: region A with a single attracting equilibrium that can take any value of \mathcal{H}_ε , and the bistability region D , where two stable equilibria coexist, one associated with \mathcal{H}_ε near 0 and the other with \mathcal{H}_ε near 1. In particular, both region B with stable oscillations, and region C , no longer exists for $\varepsilon > 0.147$. Hence, we conclude that the existence of self-sustained oscillations in the (adjusted) Welander model requires sufficiently fast switching between convective and non-convective mixing of surface water with the deep ocean.

4 Discussion and outlook

We studied the adjusted Welander model (7) with transition function \mathcal{H}_ε between weak and strong mixing between the warm surface and cold deep ocean as given by (4). This conceptual model in the context of the AMOC describes the evolution of temperature and salinity on the ocean surface in the Labrador and Nordic seas. We performed a bifurcation analysis with advanced tools from (non-smooth) dynamical systems theory, first for the piecewise-smooth limiting case $\varepsilon = 0$ when \mathcal{H}_0 is the Heaviside function, and then for the smooth case of \mathcal{H}_ε with small $\varepsilon > 0$. Specifically, we presented bifurcation diagrams in the (μ, η) -plane of salinity versus temperature flux ratio μ and density threshold η , where the rates κ_1 of weak (non-convective) and κ_2 of strong (convective) mixing were fixed at suitable values. For the PWS model with $\varepsilon = 0$, all curves of codimension-one bifurcations and points of codimension-two bifurcations were determined analytically — resulting in a complete description of all possible dynamics and the transitions between them. In this way, we identified the respective discontinuity-induced bifurcations, including the continuum of homoclinic orbits investigated in [24], and showed how these are generated or lost as μ and η change along different paths. In fact, the bifurcation diagram in the (μ, η) -plane we presented for this case is complete and representative: it does not change in a qualitative way when a different choice is made for $0 < \kappa_1 < \kappa_2$, as the expressions we derived show. For the smooth case, we computed the corresponding bifurcation diagram in the (μ, η) -plane for $\varepsilon = 0.1$ by means of numerical continuation. While the bifurcation diagram is complete, we concentrated here on four main regions of dynamics. In particular, we identified the region with oscillations found in Welander’s original model [20], as well as a region of bistability that resembles previously described dynamics in a hierarchy of AMOC models [8].

We also performed a partial bifurcation analysis in (μ, η, ε) -space for small values of ε , which focused on surfaces of Hopf and saddle-node bifurcations that (effectively) bound the main regions. In this way, we showed how the bifurcation diagram for $\varepsilon > 0$ is ‘connected’ to that of the PWS limit. Here, the switching time ε plays the role of a parameter that desingularises the limiting Heaviside switching function for $\varepsilon = 0$. A direction for future mathematical work would be to use tools from geometric singular perturbation theory [37] to study via slow-fast regularisation [38] how complicated smooth dynamics arises from the piecewise-linear limit. In this context, we conjecture that the family of homoclinic orbits along the segment \widehat{BE}_1^P will generate a singular Hopf bifurcation with subsequent canard explosion to the Welander-type large periodic orbit — with the maximally sliding orbit γ_1^* being the limit of a maximal canard [39].

Returning to the context of the AMOC, we found for large influxes of freshwater (smaller μ) that mixing is dominantly non-convective, with the system approaching a stable equilibrium associated with κ_1 . Conversely, the mixing is dominated by convection for large influxes of salinity (larger μ), with convergence to a stable equilibrium associated with κ_2 . We found that the intermediate region of bistability in the AMOC strength exists throughout and is rather independent of the switching time

parameter ε . In contrast, the region of oscillations, where the AMOC strength changes periodically between strong and weak, does depend on ε . In fact, oscillations are present only for sufficiently small ε : when the switching between the two regimes of mixing regimes becomes too slow, oscillations are no longer observed.

More generally, the investigation of a conceptual model, such as system (7), is a tool to uncover and highlight possible types of dynamics one may observe in the the AMOC. Specifically, we considered here the issue of deep ocean mixing in the North Atlantic in isolation from the larger climate system. Of course, there are many other climate processes that influence the overall state of the AMOC, and the analysis presented should be seen as forming a basis for the investigation of possible extensions of the model. There are several interesting directions for future research in this regard, all with their own mathematical challenges. One option is to consider additional boxes in the model, such as an Equatorial box as in Stommel’s original setup [18], or even to model the two deep-water convection sites in the Labrador sea and the Nordic seas by separate boxes as in [21]; indeed, such models are of higher dimensions, which makes their bifurcation analysis more involved. Another direction is to incorporate seasonal changes, for example, by periodic forcing the freshwater influx parameter μ , which leads to a non-autonomous model. Finally, the AMOC displays a number of feedback loops, such as the salt-advection into the subpolar North Atlantic. Incorporating feedback loops leads to the study of conceptual climate models in the form of delay differential equations, the study of which is possible but challenging because they have an infinite-dimensional phase space [40].

Acknowledgements

This work was supported in part by Royal Society Te Apārangi Marsden Fund grant #19-UOA-223. We thank Henk Dijkstra for many helpful discussion, especially regarding the form of the adjusted Welander model we study here.

A Proofs of Propositions 1–4

We now state and then verify the required properties for the specific case of system (8), with reference to the literature on planar Filippov systems where applicable. For in-depth background on general Filippov system theory and the associated formalism see [30, 31].

Proof of Proposition 1 (Sliding segments and tangency points).

The linear switching manifold Σ is given as the zero set of the switching function $g(x, y) = y - x - \eta$, and it has the constant normal vector $\mathbf{n} = \begin{pmatrix} -1 \\ 1 \end{pmatrix}$. A tangency point F_i occurs when $(f_i \cdot \mathbf{n})(x, y) = 0$ (more generally, when the first Lie derivative of g with respect to f_i is zero [30]). With $y = x + \eta$ on Σ we obtain

$$(f_i \cdot \mathbf{n})(x, x + \eta) = x - 1 + \mu - \eta\kappa_i, \quad (29)$$

which yields (13). The visibility of the tangency point F_i , when it is quadratic, is determined by the curvature of the orbit of f_i from F_i relative to Σ . This is measured by the second Lie derivative of g with respect to f_i [30], which for system (8) is given by

$$(f_i \cdot \nabla(f_i \cdot \mathbf{n}))(x, y) = (1 + \kappa_i)(1 - (1 + \kappa_i)x) - \kappa_i\mu + \kappa_i^2y,$$

where ∇ is the gradient. Evaluating at F_i gives

$$(f_i \cdot \nabla(f_i \cdot \mathbf{n}))(F_i) = \mu + \kappa_i(\mu - \eta - 1) - \eta\kappa_i^2,$$

which yields the genericity condition (14), and the visibility conditions (15) and (16).

The tangency points F_1 and F_2 bound Σ_s and (29) implies

$$(f_1 \cdot \mathbf{n})(x, x + \eta) > 0 \text{ for } x > F_1 \quad \text{and} \quad (f_2 \cdot \mathbf{n})(x, x + \eta) < 0 \text{ for } x < F_2.$$

From (13) we know that $F_1 < F_2$ for $\eta > 0$, while $F_2 < F_1$ for $\eta < 0$, which yields (17) and (18). \square

Proof of Proposition 2 (Equilibria, sliding vector field and pseudo-equilibria).

1. Expression (19) immediately follow from setting $f_i(x, y) = 0$, and conditions (20) and (21) are immediate consequences from the definition of R_i in (11) and (12), respectively. The Jacobian

$$J_{f_i}(x, y) = \begin{bmatrix} -(1 + \kappa_i) & 0 \\ 0 & -\kappa_i \end{bmatrix} \quad (30)$$

of f_i has two negative real eigenvalues $\lambda_{ss} = -(1 + \kappa_i)$ and $\lambda_s = \kappa_i$, which implies that p_i is a stable node. Since λ_{ss} has eigenvector $\begin{pmatrix} 1 \\ 0 \end{pmatrix}$, the statement on $W_{loc}^{ss}(p_i)$ follows.

2. The sliding vector field on the line Σ_s is given by

$$f_s(x, x + \eta) = ((1 - \lambda(x))f_1 + \lambda(x)f_2)(x, x + \eta), \quad (31)$$

where $\lambda(x) \in [0, 1]$ is chosen such that the vector f_s is in the (constant) direction $\begin{pmatrix} 1 \\ 1 \end{pmatrix}$ of Σ_s . This means that both components of the vector $f_s(x, x + \eta)$ are equal, which this is the case for

$$\lambda(x) = \frac{x + \mu - \kappa_2\eta - 1}{\eta(\kappa_1 - \kappa_2)}.$$

Insertion into (31) and simplification yields f_s as given in (22).

3. Setting $f_s(x, x + \eta) = 0$ means solving the quadratic equation

$$Q(x) := \mu + (\mu - \kappa_2\eta - 1)x + x^2$$

in (22), which gives the expressions for q^\pm in (23). The stated properties follow from evaluating $\frac{dQ(x)}{dx}$ at the x -values of q^- and q^+ , respectively. \square

Proof of Proposition 3 (Codimension-one bifurcations).

1. The equilibrium p_i from Proposition 2 collides with the switching manifold Σ when

$$g(p_i) = \frac{\mu}{\kappa_i} - \frac{1}{\kappa_i + 1} - \eta = 0.$$

Solving this for η gives the stated expression for BE_1 and BE_2 . According to (13) the respective boundary equilibrium bifurcations happens at the tangency point $F_i = p_i$, and (23) shows that this involves the (dis)appearance of an admissible pseudo-equilibria through F_i . Simultaneously, there is a change in visibility of F_i [41, 31], as can be seen from (15) and (16). It follows that the visibility of the tangency points F_i and the presence of admissible pseudo-equilibria q^\pm in the different regions of the (μ, η) -plane are as stated. See Proposition 4 for details regarding genericity conditions and different manifestations of the boundary equilibrium bifurcations along the curves BE_1 and BE_2 .

2. For $\eta = 0$ we have $F^* = F_1 = F_2$ according to (13), which is the defining property of the fold-fold bifurcation FF; for genericity conditions and resulting different manifestations see Proposition 4.
3. A saddle-node bifurcation of pseudo-equilibria occurs when the square root in (23) is zero, which gives

$$\eta = -(\mu + 1) + 2\sqrt{\mu}$$

and, hence, PS as stated, and also q^* as in (24). The saddle-node is generic since $\frac{d^2Q(x)}{dx^2} = 2 \neq 0$. Since $(\mu + 1)^2 - 4\mu = (\mu - 1)^2 > 0$, we know that $\eta < 0$ along the curve PS. Hence, q^* lies on Σ_s^r with $F_2 < q^* < F_1$, and the stated bounds for μ follow. \square

Proof of Proposition 4 (Codimension-two bifurcations).

1. The expressions for FB_i follow immediately from Proposition 3 by requiring that the curve FF intersects the curves BE_1 and BE_2 , respectively, yielding $p_i = F^*$. Note that these curves intersect transversely at FB_i , and the genericity conditions for FF and BE_i are satisfied, which means that the fold-boundary equilibrium bifurcations are generic; see [42].

The points FB_i divide the fold-fold curve FF into segments FF_i , where $f_1(F^*)$ and $f_2(F^*)$ are colinear, and a segment FU where they are not. With

$$f_i \cdot \nabla(f_i \cdot \mathbf{n})(F^*) = \mu + (\mu - 1)\kappa_i,$$

we conclude that along FF_i the fold-fold bifurcation is for a visible and an invisible quadratic tangency, which is exactly the case VI_1 described in [31]. It also follows that along FU the fold-fold bifurcation is for two invisible quadratic tangencies, and with nearby flows in opposite directions; this identifies this case as a fused-focus bifurcation according to [31]. The bifurcating (crossing) periodic orbit Γ is stable as demonstrated by the phase portraits presented in Section 2.2. We remark that the stability of Γ can be determined by considering the (local) return map around F^* [30, 31], but this is beyond the scope of this paper.

The points FB_i also divide BE_i locally as stated; this follows from the change of stability of the sliding segment and the associated change from $F_1 < F_2$ for $\eta > 0$ to $F_2 < F_1$ for $\eta < 0$; see Proposition 1 and the illustrated and discussed in depth in Section 2.4.

2. At the point BB of double-boundary equilibrium bifurcation there are boundary equilibrium bifurcations simultaneously at $p_1 \neq p_2$, and its location is readily found by equating expressions in Proposition 3 for the curves BE_1 and BE_2 , which intersect transversally. It follows that the division of the curves BE_i as are stated; this is illustrated and discussed in Section 2.4.
3. The point GB_i is found by equating the expressions for the curves BE_i and PS from Proposition 3. Whether the boundary equilibrium bifurcation BE_i is of non-smooth fold or persistence type depends on the sign of the higher-order term [42]

$$(\mathbf{n} \cdot (J_{f_j})^{-1} \cdot f_i)(p_2) = \frac{1}{\kappa_j} \left(\frac{\kappa_i^2}{(\kappa_i + 1)^2} - \mu \right)$$

Here $j \neq i \in \{1, 2\}$ is the respective other index and J_{f_j} is the Jacobian from (30). Hence, a sign change for the curve BE_i happens at the point GB_i ; specifically, BE_i is of persistence type for $\mu > \frac{\kappa_i^2}{(\kappa_i + 1)^2}$ and of non-smooth fold type for $\mu < \frac{\kappa_i^2}{(\kappa_i + 1)^2}$. \square

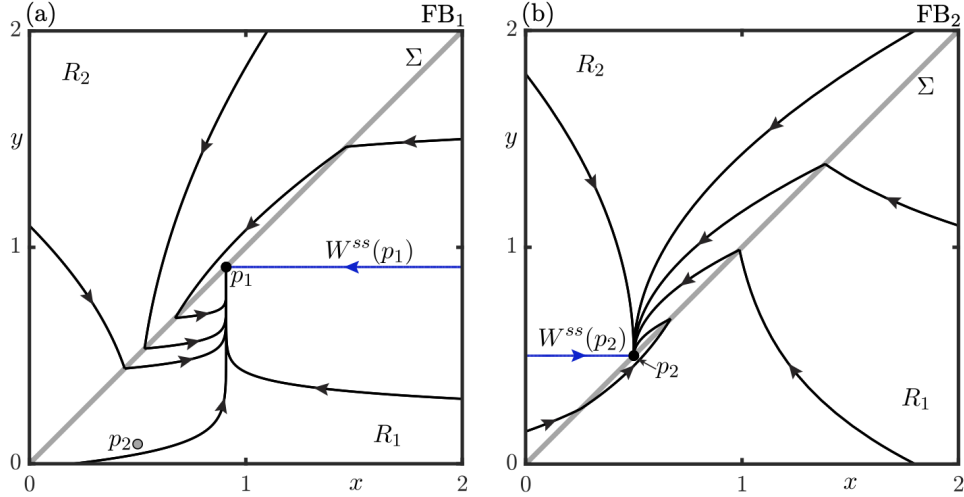


Figure 17: Representative phase portrait at codimension-two points FB_1 and FB_2 . Panel (a) for $(\mu, \eta) = (0.0909, 0)$ at FB_1 shows the globally stable boundary-node p_1 with strong stable manifold $W^{ss}(p_1)$. Panel (b) for $(\mu, \eta) = (0.5, 0)$ at FB_2 shows the globally stable boundary-node p_2 with the strong stable manifold $W^{ss}(p_2)$.

B Phase portraits at codimension-two bifurcations

We present in Figures 17 and 18 phase portraits at the points $\text{FB}_1, \text{FB}_2, \text{BB}, \text{GB}_1$ and GB_2 from Proposition 4. This illustrates how these codimension-two bifurcation points give the nearby codimension-one boundary equilibrium bifurcations BE_i and fold-fold bifurcations FF their different flavours.

Figure 17 presents phase portraits at the fold-boundary equilibrium bifurcation points FB_1 and FB_2 . The phase portrait at FB_1 is shown in panel (a). It features an attracting boundary-node p_1 that is simultaneously a singular tangency point, which is invisible for f_2 . All orbits converge to p_1 along the weak eigendirection in R_1 . The equilibrium p_2 is in R_1 and non-admissible. The phase portrait at FB_2 is shown in panel (b). The equilibrium p_2 is now the attracting boundary-node and an invisible tangency point for f_1 that attracts all orbits along the weak eigendirection in R_2 . In both cases, the strong stable manifold $W^{ss}(p_i)$ of p_i is the corresponding arriving orbit in R_i .

Figure 18 presents phase portraits at the remaining codimension two points. The phase portrait at the double boundary equilibrium bifurcation BB at the intersection of the BE_1 and BE_2 curves is shown in panel (a). It features a repelling sliding segment Σ_s^r bounded on the left by the attracting boundary node p_2 and on the right by the attracting boundary node p_1 . The pseudo-equilibria q^- and q^+ are both on Σ_c and non-admissible (and not shown): the pseudo-equilibrium q^- is at the left hand boundary p_2 , and q^+ is at the right hand boundary p_1 . There is a heteroclinic connection between p_1 and p_2 composed of orbit segments in R_1 and R_2 , respectively. Moreover, a (sliding) heteroclinic connection between the equilibria is composed of the sliding orbit from p_1 to p_2 . If we interpret the departing orbits from Σ_s^r as having a sliding component, then there is a continuum of homoclinic connections to p_1 in R_1 composed of departing orbits from Σ_s^r and a corresponding sliding component. Note that the boundary-node p_1 has a strong stable manifold $W^{ss}(p_1)$ composed of a horizontal component in R_1 . Similarly, the boundary-node p_2 also has a strong stable manifold $W^{ss}(p_2)$, composed of a horizontal component in R_2 . Overall, the boundary equilibrium bifurcations occurring simultaneously leads to a pseudo-equilibrium emerging on the sliding segment along $\widetilde{\text{BE}}_1^P$

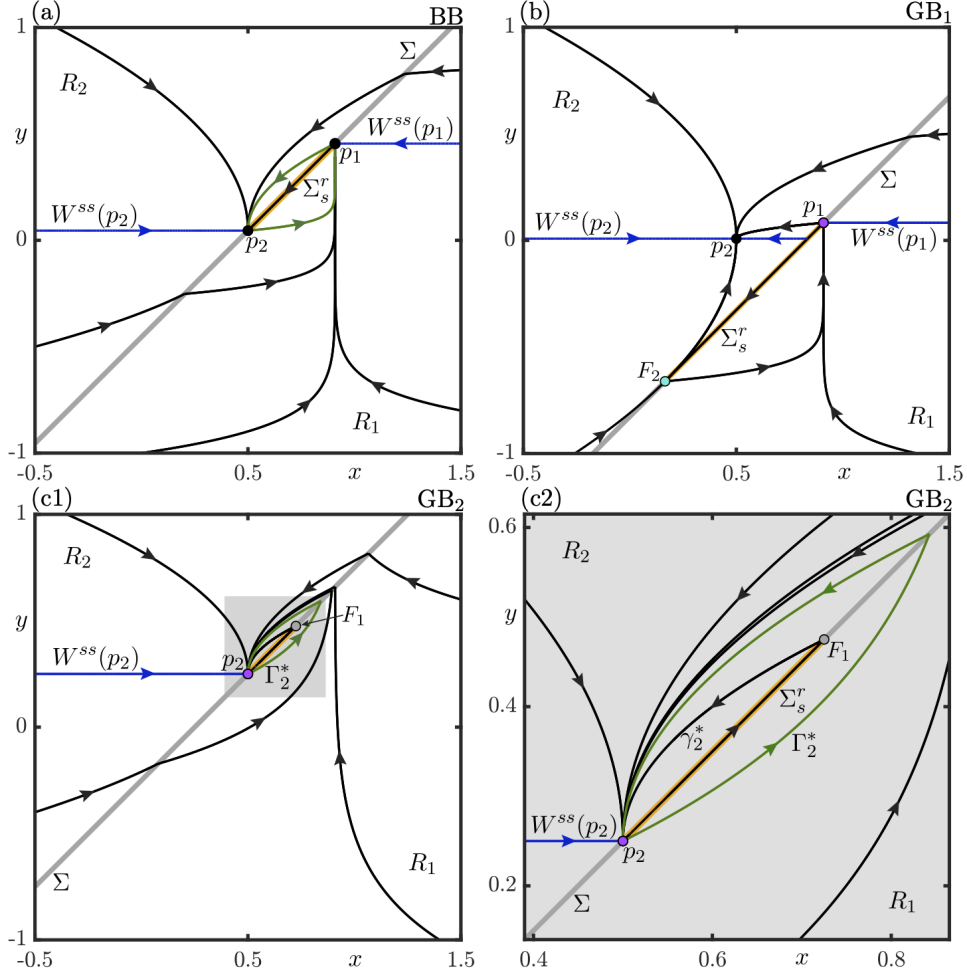


Figure 18: Representative phase portraits at codimension two points GB_2 , BB and GB_1 . Each phase portrait features a repelling sliding segment Σ_s^r . Panel (a) for $(\mu, \eta) = (0.0083, -0.8264)$ at BB shows the boundary-nodes p_1 and p_2 with corresponding strong stable manifolds $W^{ss}(p_1)$ and $W^{ss}(p_2)$. A heteroclinic connection is shown in green. Panel (b) for $(\mu, \eta) = (0.0455, -0.4545)$ at GB_1 shows the quadratic tangency point F_2 and a generalized boundary-node p_1 . The equilibrium p_2 is shown in R_2 . Panel (c1) for $(\mu, \eta) = (0.25, -0.25)$ at GB_2 and a magnification (c2) near the sliding segment shows an invisible quadratic tangency point F_1 and a generalized boundary-node p_2 with a strong stable manifold $W^{ss}(p_2)$. There are homoclinic connections to p_2 denoted Γ_2^* and γ_2^* .

and \widehat{BE}_2^F ; see Section 2.4. The phase portrait at the generalised boundary equilibrium bifurcation GB_1 is shown in panel (b). It features a repelling sliding segment Σ_s^r bounded on the left by the visible quadratic tangency point F_2 and on the right by the attracting generalised boundary-node p_1 (shown in magenta). The pseudo-equilibria q^- and q^+ undergo a pseudo-saddle-node bifurcation at the right hand boundary-node p_1 . The phase portrait at the generalised boundary equilibrium bifurcation GB_2 is shown in panel (c1) with a magnification near the sliding segment in panel (c2). The repelling sliding segment Σ_s^r is bounded on the left by generalised boundary node p_2 (shown in magenta) and on the right by the invisible quadratic tangency point F_1 . The homoclinic connections γ_2^* and Γ_2^* are the same as described in Section 2.4; see also Figure 9(b). The departing orbits from Σ_s^r together

with the respective sliding component from p_2 , form a continuum of homoclinic connections to p_2 . In particular, within γ_2^* there are homoclinic connections composed of a departing orbit from Σ_s^r in R_2 and the corresponding sliding orbit. There are also homoclinic connections inbetween γ_2^* and Γ_2^* , which feature departing orbits from Σ_s^r in R_1 that cross Σ into R_2 .

References

- [1] T. Kuhlbrodt, A. Griesel, M. Montoya, A. Levermann, M. Hofmann, S. Rahmstorf, On the driving processes of the Atlantic meridional overturning circulation, *Reviews of Geophysics* 45 (2) (2007).
- [2] K. Speer, S. R. Rintoul, B. Sloyan, The diabatic deacon cell, *Journal of Physical Oceanography* 30 (12) (2000) 3212–3222.
- [3] B. M. Sloyan, S. R. Rintoul, The southern ocean limb of the global deep overturning circulation, *Journal of Physical Oceanography* 31 (1) (2001) 143–173.
- [4] H. Jeffreys, On fluid motions produced by differences of temperature and humidity, *Quarterly Journal of the Royal Meteorological Society* 51 (216) (1925) 347–356.
- [5] J. W. Sandstrom, *Meteorologische studien im schwedischen Hochgebirge*, Goteborg Wettergren and Kerber 1916, 1916.
- [6] J. Toggweiler, B. Samuels, On the ocean’s large-scale circulation near the limit of no vertical mixing, *Journal of Physical Oceanography* 28 (9) (1998) 1832–1852.
- [7] R. Marsh, W. Hazeleger, A. Yool, E. J. Rohling, Stability of the thermohaline circulation under millennial CO₂ forcing and two alternative controls on Atlantic salinity, *Geophysical Research Letters* 34 (3) (2007).
- [8] W. Weijer, W. Cheng, S. S. Drijfhout, A. V. Fedorov, A. Hu, L. C. Jackson, W. Liu, E. McDonagh, J. Mecking, J. Zhang, Stability of the atlantic meridional overturning circulation: A review and synthesis, *Journal of Geophysical Research: Oceans* 124 (8) (2019) 5336–5375.
- [9] M. Srokosz, M. Baringer, H. Bryden, S. Cunningham, T. Delworth, S. Lozier, J. Marotzke, R. Sutton, Past, present, and future changes in the Atlantic meridional overturning circulation, *Bulletin of the American Meteorological Society* 93 (11) (2012) 1663–1676.
- [10] S. Rahmstorf, J. E. Box, G. Feulner, M. E. Mann, A. Robinson, S. Rutherford, E. J. Schaffernicht, Exceptional twentieth-century slowdown in atlantic ocean overturning circulation, *Nature Climate Change* 5 (5) (2015) 475–480.
- [11] M. Dima, G. Lohmann, Evidence for two distinct modes of large-scale ocean circulation changes over the last century, *Journal of Climate* 23 (1) (2010) 5–16.
- [12] R. R. Dickson, J. Meincke, S.-A. Malmberg, A. J. Lee, The “great salinity anomaly” in the northern North Atlantic 1968–1982, *Progress in Oceanography* 20 (2) (1988) 103–151.
- [13] L. Jackson, R. Kahana, T. Graham, M. Ringer, T. Woollings, J. Mecking, R. Wood, Global and european climate impacts of a slowdown of the AMOC in a high resolution GCM, *Climate dynamics* 45 (11) (2015) 3299–3316.

- [14] A. Schmittner, Decline of the marine ecosystem caused by a reduction in the Atlantic overturning circulation, *Nature* 434 (7033) (2005) 628–633.
- [15] M. Gregory, K. Dixon, R. Stouffer, A. Weaver, E. Driesschaert, M. Eby, T. Fichefet, H. Hasumi, A. Hu, J. Jungclauss, et al., A model intercomparison of changes in the atlantic thermohaline circulation in response to increasing atmospheric CO₂ concentration, *Geophysical Research Letters* 32 (12) (2005).
- [16] S. Nghiem, D. Hall, T. Mote, M. Tedesco, M. Albert, K. Keegan, C. Shuman, N. DiGirolamo, G. Neumann, The extreme melt across the Greenland ice sheet in 2012, *Geophysical Research Letters* 39 (20) (2012).
- [17] H. A. Dijkstra, *Nonlinear Physical Oceanography: a Dynamical Systems Approach to the Large Scale Ocean circulation and El Niño*, Vol. 28, Springer Science & Business Media, 2005.
- [18] H. Stommel, Thermohaline convection with two stable regimes of flow, *Tellus* 13 (2) (1961) 224–230.
- [19] C. Rooth, Hydrology and ocean circulation, *Progress in Oceanography* 11 (2) (1982) 131–149.
- [20] P. Welander, Thermohaline effects in the ocean circulation and related simple models, in: *Large-scale transport processes in oceans and atmosphere*, Springer, 1986, pp. 163–200.
- [21] A. Neff, A. Keane, H. A. Dijkstra, B. Krauskopf, Bifurcation analysis of a North Atlantic ocean box model with two deep-water formation sites (2023). [arXiv:2305.11975](https://arxiv.org/abs/2305.11975).
- [22] P. Welander, A simple heat-salt oscillator, *Dynamics of Atmospheres and Oceans* 6 (4) (1982) 233–242. [doi:10.1016/0377-0265\(82\)90030-6](https://doi.org/10.1016/0377-0265(82)90030-6).
- [23] H. E. Huppert, J. S. Turner, Double-diffusive convection, *Journal of Fluid Mechanics* 106 (1981) 299–329.
- [24] J. Leifeld, Nonsmooth homoclinic bifurcation in a conceptual climate model (2016). [arXiv:1601.07936](https://arxiv.org/abs/1601.07936).
- [25] P. Cessi, Convective adjustment and thermohaline excitability, *Journal of Physical Oceanography* 26 (4) (1996) 481–491.
- [26] Y. A. Kuznetsov, I. A. Kuznetsov, Y. Kuznetsov, *Elements of Applied Bifurcation Theory*, Vol. 112, Springer, 1998.
- [27] E. J. Doedel, T. F. Fairgrieve, B. Sandstede, A. R. Champneys, Y. A. Kuznetsov, X. Wang, *Auto-07p: Continuation and bifurcation software for ordinary differential equations*, Tech. rep., Concordia University (2007).
- [28] M. Bernardo, C. Budd, A. R. Champneys, P. Kowalczyk, *Piecewise-Smooth Dynamical Systems: Theory and Applications*, Vol. 163, Springer Science & Business Media, 2008.
- [29] A. F. Filippov, *Differential equations with discontinuous righthand sides: control systems*, Vol. 18, Springer Science & Business Media, 2013.
- [30] M. Guardia, T. Seara, M. A. Teixeira, Generic bifurcations of low codimension of planar Filippov systems, *Journal of Differential Equations* 250 (4) (2011) 1967–2023.

- [31] Y. A. Kuznetsov, S. Rinaldi, A. Gragnani, One-parameter bifurcations in planar Filippov systems, *International Journal of Bifurcation and Chaos* 13 (08) (2003) 2157–2188.
- [32] P. T. Piiroinen, Y. A. Kuznetsov, An event-driven method to simulate Filippov systems with accurate computing of sliding motions, *ACM Transactions on Mathematical Software (TOMS)* 34 (3) (2008) 1–24.
- [33] J. Castillo, J. Llibre, F. Verduzco, The pseudo-Hopf bifurcation for planar discontinuous piecewise linear differential systems, *Nonlinear Dynamics* 90 (3) (2017) 1829–1840.
- [34] S. H. Strogatz, *Nonlinear Dynamics and Chaos: With Applications to Physics, Biology, Chemistry and Engineering*, Westview Press, 2000.
- [35] B. Krauskopf, H. M. Osinga, A codimension-four singularity with potential for action, in: *Mathematical Sciences with Multidisciplinary Applications*, Springer, 2016, pp. 253–268.
- [36] F. Dumortier, R. Roussarie, J. Sotomayor, H. Zoladek, *Bifurcations of Planar Vector Fields: Nilpotent Singularities and Abelian Integrals*, Springer, 2006.
- [37] C. K. R. T. Jones, *Geometric Singular Perturbation Theory, Dynamical systems (Montecatini Terme, 1994)*, Springer-Verlag, Berlin/New York, 1995.
- [38] M. Jeffrey, D. Duarte Novaes, Regularization of hidden dynamics in piecewise smooth flows, *Journal of Differential Equations* 259 (9) (2015) 4615–4633.
- [39] M. Desroches, J. Guckenheimer, B. Krauskopf, C. Kuehn, H. Osinga, M. Wechselberger, Mixed-mode oscillations with multiple time scales, *SIAM Review* 54 (2) (2012) 211–288.
- [40] A. Keane, B. Krauskopf, C. M. Postlethwaite, Climate models with delay differential equations, *Chaos* 27 (11) (2017) 114309.
- [41] M. Di Bernardo, A. Nordmark, G. Olivar, Discontinuity-induced bifurcations of equilibria in piecewise-smooth and impacting dynamical systems, *Physica D: Nonlinear Phenomena* 237 (1) (2008) 119–136.
- [42] F. Della Rossa, F. Dercole, Generalized boundary equilibria in n-dimensional Filippov systems: The transition between persistence and nonsmooth-fold scenarios, *Physica D: Nonlinear Phenomena* 241 (22) (2012) 1903–1910.